Alternative approaches of evaluating Diffraction Transfer Matrix and Radiation Characteristics using the hybrid source-dipole formulation

Liu, Yingyi
Research Institute for Applied Mechanics, Kyushu University

Liang, Hui
Technology Centre for Offshore and Marine, Singapore (TCOMS)

Kashiwagi, Masashi
Department of Naval Architecture and Ocean Engineering, Graduate School of Engineering, Osaka University

Cong, Peiwen
State Key Laboratory of Coastal and Offshore Engineering, Dalian University of Technology

出版情報：Applied Ocean Research. 114 (102769), 2021-09. Elsevier
バージョン：

Applied Ocean Research 114 (2021) 102769

Contents lists available at ScienceDirect

Applied Ocean Research

journal homepage: www.elsevier.com/locate/apor

Alternative approaches of evaluating Diffraction Transfer Matrix and Radiation Characteristics using the hybrid source-dipole formulation

Yingyi Liu [*,a], Hui Liang [b], Masashi Kashiwagi [c], Peiwen Cong [d]

[a] Research Institute for Applied Mechanics, Kyushu University, Fukuoka 8168580, Japan
[b] Technology Centre for Offshore and Marine, Singapore (TCOMS), 118411, Singapore
[c] Department of Naval Architecture and Ocean Engineering, Graduate School of Engineering, Osaka University, Osaka 5650871, Japan
[d] State Key Laboratory of Coastal and Offshore Engineering, Dalian University of Technology, Dalian 116024, China

ARTICLE INFO

Keywords:
Multiple scattering
Wave interaction
Polar Green's function
Finite water depth
Wave energy converters

ABSTRACT

The interaction theory presented by Kagemoto and Yue (1986) significantly reduces the computational burden in the wave interaction problem of multiple surface-piercing bodies, particularly arrays of wave energy converters in recent years. Two essential operators of the theory are the so-called Diffraction Transfer Matrix and Radiation Characteristics. Many subsequent researchers (Goo and Yoshida, 1990; Flavià et al., 2018) have implemented the theory using the source distribution method in evaluating the two linear operators of a single unique geometry. However, nowadays, a great majority of boundary element method codes have been written by virtue of the hybrid source-dipole distribution method on account of its high accuracy. In this regard, the present work aims to introduce a full set of mathematical formulations, as well as a complete derivation process of evaluating the two operators based on the hybrid source-dipole distribution method. The proposed formulations are then applied to two benchmark geometries, as given by McNatt et al. (2015) and Flavià et al. (2018). Good agreement is found between the present results and those from the literature. Moreover, two alternative approaches to solve the diffraction problem have been compared to assess both their accuracy and efficiency. It is found that the two methods present similar levels of accuracy but very different computational burden.

1. Introduction

Wave loads are of primary concern during the lifetime of a marine structure in the real sea environment. On the one hand, wave interaction with marine structures has been a continuous interest to the researchers and engineers of the ocean and offshore engineering community. On the other hand, along with the development of computational technology, great progress has been witnessed in the prediction of wave loads on multiple bodies, such as the interconnected multi-moduled floating offshore structure (Chakrabarti, 2001), ice-floes in the marginal ice zone (Peter and Meylan, 2004b; Bennetts and Squire, 2009), and very-large floating structures (Kashiwagi, 2000; 2001; 2017), etc. In particular, a broad interest has been focused on arrays of wave energy converters or wave farms in recent years (Göteman et al., 2015; Sun et al., 2016; Göteman, 2017; Zhong and Yeung, 2019; Zheng et al., 2018; Zheng et al., 2020), in which analytical approaches or semi-analytical approaches applying the multiple-scattering interaction theory have been extensively used.

The multiple-scattering interaction theory was first brought into the water-wave problem by Ohkusu (1974), who extended it from the acoustic radiation analysis of arrays of two-dimensional circular cylinders by Twersky (1952). Kagemoto and Yue (1986) combined it with the Direct Matrix Method (Spring and Monkmeyer, 1974; Simon, 1982; McIver and Evans, 1984; McIver, 1984), and developed an exact interaction theory, and applied it to axisymmetric bodies. Goo and Yoshida (1990) enabled the method of Kagemoto and Yue (1986) for computation of arbitrary geometrical bodies by taking advantage of the source distribution panel method and the Green function in polar coordinates (Black, 1975; Fenton, 1978; Hulme, 1983). Thereafter, the improved Direct Matrix Method has been widely applied to offshore and marine applications. Meanwhile, further extensions were successfully made by Peter and Meylan (2004b) to the interaction theory in infinite-depth water, and Kashiwagi (2000) to hierarchical interaction theory in multiple layers. In the recent decade, the interaction theory was used for the wave energy converters in arrays (Child and Venugopal, 2010; Göteman et al., 2015; McNatt et al., 2015), as well as for multi-body WECs

* Corresponding author.
E-mail addresses: liuyingyi@riam.kyushu-u.ac.jp (Y. Liu), liang_hui@tcoms.sg (H. Liang), kashi@naoe.eng.osaka-u.ac.jp (M. Kashiwagi), pwcong@dlut.edu.cn (P. Cong).

https://doi.org/10.1016/j.apor.2021.102769
Received 18 December 2020; Received in revised form 3 June 2021; Accepted 24 June 2021
Available online 5 July 2021

composed of a large number of floats (Flavià et al., 2017), in which the majority of geometries are regular and having analytical solutions. Due to the reason that method of Goo and Yoshida (1990) requires the modification of a BEM solver for the body boundary conditions, it is not possible to do that without access to the source code of the BEM solver. McNatt et al. (2015), therefore, developed an alternative method that can derive the Diffraction Transfer Matrix (DTM) and the Radiation Characteristics (RC) from the standard output of wave potentials (indeed wave dynamic pressures and elevations) of a BEM solver, with only the progressive mode but without the evanescent modes. Later, Flavià et al. (2018) implemented the method of Goo and Yoshida (1990) on the open-source BEM code Nemoh (Babarit and Delhommeau, 2015) and also derived general identities to water-wave multiple-scattering problems (Flavià and Meylan, 2019).

From a mathematical point of view, the multiple-scattering interaction theory is primarily based on a mathematical theorem, i.e., Graf's addition theorem (Abramowitz and Stegun, 1964), which is a special case of a general addition theorem called Neumann's addition theorem (Meylan, 2007 (accessed on Oct. 12, 2020). With the aid of Grafs addition theorem for Bessel functions, influence between two spatial points can be translated onto those involving a third spatial point. Thanks to this characteristic, the wave potentials (including the source potential, i.e., the free-surface Green function) are possible to be expressed in polar coordinates as an expansion of the Fourier series. The source potential expressed in this form is usually referred to as the 'ring source' (Hulme, 1983), which has been extensively applied in calculating higher-order waves loads on offshore structures (Chau, 1989; Kim and Yue, 1989; Cong et al., 2012; Teng and Cong, 2017, etc.).

It is worth mentioning that, so far, many conventional applications of the multiple-scattering interaction theory in a BEM (Goo and Yoshida, 1990; Chakrabarti, 2001; Peter and Meylan, 2004a; Flavià et al., 2018) have been based on the source distribution method (i.e., the source formulation). The source formulation has the advantage of easy evaluation of the fluid velocity. However, it was proved to be less accurate than the hybrid source-dipole distribution method (i.e., the potential formulation) in evaluating the wave potentials (Dai and Duan, 2008). Besides, the potential formulation may be more versatile, particularly in representing thin plates or shell structures with elements (Lee and Newman, 2005). Due to these reasons, quite a few BEM solvers have been developed based on the potential formulation, such as WAMIT (Lee, 1995), DIFFRACT (Eatock Taylor and Chau, 1992), WAFDUT (Teng and Eatock Taylor, 1995), HAMS (Liu, 2019), etc. Unfortunately, rare work has covered the topic of numerical implementation of the two essential operators for the potential formulation up to date. In addition to that, by using the potential formulation, one can choose to solve the scattering potential using the conventional method and then obtain the diffraction potential, or solve directly the diffraction potential by applying the incident-wave potential as the forcing term on the right-hand side of the boundary integral equation. The two ways are basically similar in wave analysis with a single body (Lee and Newman, 2005) in accuracy, but the latter one runs a bit faster than the first because there is no need to evaluate the normal derivative and its integration over the wetted surface. However, when being applied to a multi-body problem, since the right-hand side of the boundary integral equation needs to be evaluated for hundreds and thousands of times, the difference of computation time can be increased substantially. In this regard, it is necessary to check how this difference could be, such that the equivalence of the two alternative approaches may need to be reappraised.

The present work aims to systematically introduce the implementation details of the method by Kagemoto and Yue (1986) in evaluating the DTM and RC, when a BEM solver based on the potential formulation is to be used. The remaining part of the paper is therefore organized into the following sections: The mathematical theory and numerical modeling are introduced in Section 2. The full set of derivations are given for DTM and RC, which can be evaluated using alternative methods, in association with the removal of irregular frequencies encountered in the numerical implementation. The overall computation process is introduced in Section 3. Verifications of the present method and the comparative studies are given in Section 4. Conclusions are drawn in Section 5 based on the preceding analysis.

2. Mathematical theory and numerical modeling

2.1. Hybrid source-dipole boundary integral equation

Wave radiation and diffraction of an arbitrary-geometric three-dimensional floating structure can be solved by the boundary integral equation method. Based on the assumption that the fluid is inviscid, incompressible, and with an irrotational motion, the fluid flow can be described by an ideal velocity potential satisfying the Laplace equation. In a steady state, the velocity potential is written as $\phi(\boldsymbol{x},\ t) = \mathrm{Re}[\varphi(\boldsymbol{x})\mathrm{e}^{-\mathrm{i}\omega t}]$, where ω denotes the angular frequency of oscillation, and t is time. Applying Green's second identity, a Fredholm integral equation of the second kind can be constructed:

$$C(\boldsymbol{x})\varphi_k(\boldsymbol{x}) + \iint_{S_B} \varphi_k(\boldsymbol{\xi})\frac{\partial G(\boldsymbol{x},\boldsymbol{\xi})}{\partial n_{\boldsymbol{\xi}}}\mathrm{d}S = \iint_{S_B} V(\boldsymbol{\xi})G(\boldsymbol{x},\boldsymbol{\xi})\mathrm{d}S \quad \text{with} \quad k = 1, 2, ..., 7, \tag{1}$$

where $\boldsymbol{x} = (x, y, z)$ and $\boldsymbol{\xi} = (\xi, \eta, \zeta)$ represent the field point and the source point, respectively; $C(\boldsymbol{x})$ is referred to as 'solid angle coefficient', whose value depends on the local geometric shape; $G(\boldsymbol{x}, \boldsymbol{\xi})$ is the free-surface Green function. Neumann boundary conditions prescribe the normal velocity of the fluid on the immersed, impermeable body surface S_B which can be represented by

$$V(\boldsymbol{\xi}) = \begin{cases} n_k(\boldsymbol{\xi}) & k = 1 \sim 6, \\ -\dfrac{\partial \varphi_0(\boldsymbol{\xi})}{\partial n_{\boldsymbol{\xi}}} & k = 7, \end{cases} \tag{2}$$

where $n_k(\boldsymbol{\xi})$ denotes the normals on the geometrical surface and $\varphi_k(\boldsymbol{\xi})$ stands for (i) the known incident wave potential when $k = 0$, (ii) the radiation potentials when $k = 1 \sim 6$, and (iii) the scattering potential when $k = 7$. As Eq. (1) consists of both source and dipole, it is dubbed hybrid source-dipole formulation to distinguish from the source-only formulation.

2.2. Green's function in polar coordinates

It is well-known that the free-surface Green function in Eq. (1) has an eigenfunction expansion (John, 1950)

$$G = 2\pi \mathrm{i} C_0 \cosh k(z+h)\cosh k(\zeta+h)H_0^{(1)}(kL) + 4 \times \sum_{n=1}^{\infty} C_n \cos k_n(z+h)\cos k_n(\zeta+h)K_0(k_nL), \tag{3}$$

where $H_0^{(1)}(\cdot)$ is the zeroth-order Hankel function of the first kind; $K_0(\cdot)$ is the zeroth-order modified Bessel function of the second kind; L is the horizontal distance between $\boldsymbol{x}$ and $\boldsymbol{\xi}$; the expansion coefficients can be subsequently evaluated as

$$C_0 = \frac{1}{2}\left[\int_{-h}^{0} \cosh^2 k(z+h)\mathrm{d}z\right]^{-1} = \frac{k^2 - K^2}{\left(k^2 - K^2\right)h + K} = \frac{2k}{2kh + \sinh 2kh}, \tag{4}$$

$$C_n = \frac{1}{2}\left[\int_{-h}^{0} \cos^2 k_n(z+h)\mathrm{d}z\right]^{-1} = \frac{k_n^2 + K^2}{\left(k_n^2 + K^2\right)h - K} = \frac{2k_n}{2k_nh + \sin 2k_nh}, \tag{5}$$

where $K = \omega^2/g$, and k_n ($n = 0, 1, 2\ldots$) are the roots of the wave dispersion equation in finite-depth water (see Appendix A).

Eq. (3) can be expressed in polar coordinates in terms of $\boldsymbol{x} = (x, y, z) = (r\cos\theta, r\sin\theta, z)$ and $\boldsymbol{\xi} = (\xi, \eta, \zeta) = (R\cos\Theta, R\sin\Theta, \zeta)$ following Black (1975), Fenton (1978), and Hulme (1983), in the form of

$$G = 2\pi i C_0 \cosh k(z+h)\cosh k(\zeta+h)\sum_{m=-\infty}^{\infty}\left\{\frac{J_m(kR)H_m^{(1)}(kr)}{H_m^{(1)}(kR)J_m(kr)}\right\}e^{im(\theta-\Theta)} + 4\sum_{n=1}^{\infty} C_n \cos k_n(z+h)\cos k_n(\zeta+h)\sum_{m=-\infty}^{\infty}\left\{\frac{I_m(k_nR)K_m(k_nr)}{K_m(k_nR)I_m(k_nr)}\right\}e^{im(\theta-\Theta)}. \tag{6}$$

The upper terms in the curly braces are used when $r \geq R$ (the region outside of a circular cylinder that circumscribes the body or bodies) and the lower terms when $r < R$. The detailed procedure of derivation is attached as well in Appendix A. The Green function in Eq. (6) was referred to as 'ring source' by Hulme (1983).

2.3. Partial waves in cylindrical harmonics

In a finite-sized array of floating bodies, it is convenient to express the velocity potentials as the scalar product between a vector of complex coefficients and a vector of partial cylindrical wave component (McNatt et al., 2013, Flavià et al., 2018):

$$\phi_j^I = \left\{A_j^I\right\}^T\left\{\varphi_j^I\right\}, \quad \phi_j^S = \left\{A_j^S\right\}^T\left\{\varphi_j^S\right\}, \quad \phi_j^{R,k} = \{A_j^{R,k}\}^T\{\varphi_j^{R,k}\}, \tag{7}$$

where the superscript T represents the matrix transpose operator, the curly brace $\{\cdot\}$ stands for a vector and the subscript j denotes the jth body. $\{A_j^I\}$, $\{A_j^S\}$ and $\{A_j^{R,k}\}$ are the complex incident, scattered and radiated vectors of partial wave coefficients. Following the notations of Flavià et al. (2018), indexes (l,q) are associated with incident waves and (n,m) with outgoing waves. The vectors of the incident and scattered cylindrical functions are respectively expressed as

$$\left\{\varphi_j^I\right\}_{lq} = \begin{cases} \dfrac{\cosh k(z_j+h)}{\cosh kh}J_q(kr_j)e^{iq\theta_j} & l=0, \\ \cos k_l(z_j+h)I_q(k_lr_j)e^{iq\theta_j} & l\geq 1, \end{cases} \tag{8}$$

$$\left\{\varphi_j^S\right\}_{nm} = \{\varphi_j^{R,k}\}_{nm} = \begin{cases} \dfrac{\cosh k(z_j+h)}{\cosh kh}H_m^{(1)}(kr_j)e^{im\theta_j} & n=0, \\ \cos k_n(z_j+h)K_m(k_nr_j)e^{im\theta_j} & n\geq 1. \end{cases} \tag{9}$$

It is noted that the first terms of the incident and scattered cylindrical functions represent the propagating mode, while the rest terms are associated with evanescent modes.

2.4. Derivation of diffraction transfer matrix

Derivation of the DTM of a specific floating body can be started from considering the wave diffraction by a single body. The scattering potential of a single floating body in a partial incident wave of mode (l,q) without the presence of other bodies can be expressed as

$$\left[\varphi_j^S(r_j,\theta_j,z_j)\right]_{lq} = \frac{\cosh k(z_j+h)}{\cosh kh}\sum_{m=-\infty}^{\infty} D_{0m}^{j,lq}H_m^{(1)}(kr_j)e^{im\theta_j} + \sum_{n=1}^{\infty}\cos k_n(z_j+h)\sum_{m=-\infty}^{\infty} D_{nm}^{j,lq}K_m(k_nr_j)e^{im\theta_j}, \tag{10}$$

where $D_{0m}^{j,lq}$ and $D_{nm}^{j,lq}$ are scattered complex coefficients. On the other hand, the scattering potential at a field point in the fluid domain (other than the body surface) can be determined by the following equation

$$\left[\varphi_j^S(r_j,\theta_j,z_j)\right]_{lq} = -\frac{1}{4\pi}\left\{\iint_{S_B^j}\left[\varphi_j^S(R_j,\Theta_j,\zeta_j)\right]_{lq}\frac{\partial G(r_j,\theta_j,z_j;R_j,\Theta_j,\zeta_j)}{\partial n_\xi}dS + \iint_{S_B^j} G(r_j,\theta_j,z_j;R_j,\Theta_j,\zeta_j)\frac{\partial\left[\varphi_j^I(R_j,\Theta_j,\zeta_j)\right]_{lq}}{\partial n_\xi}dS\right\} \tag{11}$$

Substituting Eq. (6) into Eq. (11) and comparing Eq. (10) with Eq. (11) yields

$$D_{0m}^{j,lq} = -\frac{i}{2}C_0\cosh kh\iint_{S_B^j}\left[\left(\varphi_j^S\right)_{lq}\frac{\partial}{\partial n} + \frac{\partial\left(\varphi_j^I\right)_{lq}}{\partial n}\right]\left[J_m(kR_j)\cosh k(\zeta_j+h)e^{-im\Theta_j}\right]dS, \tag{12}$$

$$D_{nm}^{j,lq} = -\frac{1}{\pi}C_n\iint_{S_B^j}\left[\left(\varphi_j^S\right)_{lq}\frac{\partial}{\partial n} + \frac{\partial\left(\varphi_j^I\right)_{lq}}{\partial n}\right]\left[I_m(k_nR_j)\cos k_n(\zeta_j+h)e^{-im\Theta_j}\right]dS, \tag{13}$$

where $D_{0m}^{j,lq}$ and $D_{nm}^{j,lq}$ are exactly the elements of DTM. The only unknown in Eqs. (12) and (13) is $(\varphi_j^S)_{lq}$, which can be solved by the following boundary integral equation

$$2\pi\left[\varphi_j^S(r_j,\theta_j,z_j)\right]_{lq} + \iint_{S_B^j}\left[\varphi_j^S(R_j,\Theta_j,\zeta_j)\right]_{lq}\frac{\partial G(r_j,\theta_j,z_j;R_j,\Theta_j,\zeta_j)}{\partial n_\xi}dS = -\iint_{S_B^j}\frac{\partial\left[\varphi_j^I(R_j,\Theta_j,\zeta_j)\right]_{lq}}{\partial n_\xi}G(r_j,\theta_j,z_j;R_j,\Theta_j,\zeta_j)dS. \tag{14}$$

For convenience, the method of Eqs. (11) – (14) is denoted as 'Method I' hereafter.

A second way of evaluating the DTM elements is to consider the following boundary integral equation, which was first proposed by (Kashiwagi and Kohjo, 1995) and later presented in (Kashiwagi, 2000):

$$C(r_j,\theta_j,z_j)\left[\varphi_j^D(r_j,\theta_j,z_j)\right]_{lq} + \iint_{S_B^j}\left[\varphi_j^D(R_j,\Theta_j,\zeta_j)\right]_{lq}\times\frac{\partial G(r_j,\theta_j,z_j;R_j,\Theta_j,\zeta_j)}{\partial n_\xi}dS = 4\pi\left[\varphi_j^I(r_j,\theta_j,z_j)\right]_{lq}, \tag{15}$$

where $(\varphi_j^D)_{lq}$ is the total diffraction potential in correspondence to the partial incident wave of mode (l,q). At an arbitrary field point in the fluid domain, the 'solid angle coefficient' $C(r_j,\theta_j,z_j)$ is equal to 4π. Hence the scattering potential can be evaluated as

$$\left[\varphi_j^S(r_j,\theta_j,z_j)\right]_{lq} = \left[\varphi_j^D(r_j,\theta_j,z_j)\right]_{lq} - \left[\varphi_j^I(r_j,\theta_j,z_j)\right]_{lq} = -\frac{1}{4\pi}\iint_{S_B^j}\left[\varphi_j^D(R_j,\Theta_j,\zeta_j)\right]_{lq}\frac{\partial G(r_j,\theta_j,z_j;R_j,\Theta_j,\zeta_j)}{\partial n_\xi}dS, \tag{16}$$

Detailed derivations of Eq. (15) are summarized in Appendix B. Using Eq. (6) in Eq. (16) and comparing Eq. (10) with Eq. (16) yields

$$D_{0m}^{j,lq} = -\frac{i}{2}C_0\cosh kh\iint_{S_B^j}\left[\left(\varphi_j^S\right)_{lq} + \left(\varphi_j^I\right)_{lq}\right]\frac{\partial}{\partial n}\left[J_m(kR_j)\cosh k(\zeta_j+h)e^{-im\Theta_j}\right]dS, \tag{17}$$

$$D_{nm}^{j,lq} = -\frac{1}{\pi}C_n \int\int_{S_B^j} \left[\left(\varphi_j^S\right)_{lq} + \left(\varphi_j^I\right)_{lq}\right] \frac{\partial}{\partial n}\left[I_m(k_nR_j)\cosh k_n(\zeta_j+h)\mathrm{e}^{-\mathrm{i}m\Theta_j}\right]\mathrm{d}S, \tag{18}$$

Although the only unknown $(\varphi_j^S)_{lq}$ in Eqs. (17) and (19) can be solved by either Eq. (14) or Eq. (15), the latter is more computationally efficient. The method of Eqs. (15) – (18) is denoted as 'Method II' hereafter.

2.5. Derivation of radiation characteristics

The radiation potential of a single floating body of mode (n,m) without the influence of other bodies can be expressed as

$$\begin{aligned}\left[\varphi_j^{R,k}(r_j,\theta_j,z_j)\right]_{nm} = \ & \frac{\cosh k(z_j+h)}{\cosh kh}\sum_{m=-\infty}^{\infty} R_{0m}^{j,k}H_m^{(1)}(kr_j)\mathrm{e}^{\mathrm{i}m\theta_j} \\ & + \sum_{n=1}^{\infty}\cos k_n(z_j+h)\sum_{m=-\infty}^{\infty} R_{nm}^{j,k}K_m(k_nr_j)\mathrm{e}^{\mathrm{i}m\theta_j},\end{aligned} \tag{19}$$

where $R_{0m}^{j,k}$ and $R_{nm}^{j,k}$ are radiated complex coefficients in a kth rigid mode of motion ($k = 1 \sim 6$). On the other hand, the radiation potential at a field point in the fluid domain (other than the body surface) can be determined by the following equation

$$\begin{aligned}\left[\varphi_j^{R,k}(r_j,\theta_j,z_j)\right]_{lq} = -\frac{1}{4\pi}\Bigg\{ & \int\int_{S_B^j}\left[\varphi_j^{R,k}(R_j,\Theta_j,\zeta_j)\right]_{lq}\frac{\partial G(r_j,\theta_j,z_j;R_j,\Theta_j,\zeta_j)}{\partial n_\xi}\mathrm{d}S \\ & - \int\int_{S_B^j} n_{j,k}G(r_j,\theta_j,z_j;R_j,\Theta_j,\zeta_j)\mathrm{d}S\Bigg\}.\end{aligned} \tag{20}$$

Using Eq. (6) in Eq. (20), and comparing Eq. (19) with Eq. (20), leads to

$$R_{0m}^{j,k} = -\frac{\mathrm{i}}{2}C_0\cosh kh\int\int_{S_B^j}\left(\varphi_j^{R,k}\frac{\partial}{\partial n} - n_{j,k}\right)\left[J_m(kR_j)\cosh k(\zeta_j+h)\mathrm{e}^{-\mathrm{i}m\Theta_j}\right]\mathrm{d}S, \tag{21}$$

$$R_{nm}^{j,k} = -\frac{1}{\pi}C_n\int\int_{S_B^j}\left(\varphi_j^{R,k}\frac{\partial}{\partial n} - n_{j,k}\right)\left[I_m(k_nR_j)\cosh k_n(\zeta_j+h)\mathrm{e}^{-\mathrm{i}m\Theta_j}\right]\mathrm{d}S, \tag{22}$$

where $R_{0m}^{j,k}$ and $R_{nm}^{j,k}$ are exactly the elements of RC. The only unknown in Eqs. (21) and (22) is $\varphi_j^{R,k}$, which can be solved by the following boundary integral equation

$$\begin{aligned}2\pi\varphi_j^{R,k}(r_j,\theta_j,z_j) \ & + \int\int_{S_B^j}\varphi_j^{R,k}(R_j,\Theta_j,\zeta_j)\frac{\partial G(r_j,\theta_j,z_j;R_j,\Theta_j,\zeta_j)}{\partial n_\xi}\mathrm{d}S \\ & = \int\int_{S_B^j} n_{j,k}G(r_j,\theta_j,z_j;R_j,\Theta_j,\zeta_j)\mathrm{d}S.\end{aligned} \tag{23}$$

2.6. Removal of irregular frequencies

Directly solving Eq. (14), Eq. (15), or Eq. (23) can lead to some unphysical numerical distortions in the computation results around the eigen-frequencies of the eigen modes associated with Dirichlet-type boundary condition inside the floating body, which is normally called as the 'irregular frequencies' phenomenon. Most recently, Liang et al. (2020) compared the two most-effective methods for removal of these 'irregular frequencies' and concluded that using the 'overdetermined integral equations' can be a superior option rather than using the 'extended integral equations'. Hence the former method (see also: Ohmatsu, 1983; Lau and Hearn, 1989; Liu, 2019) is adopted in the present study. The supplemental boundary integral equations for Eq. (14), Eq. (15), and Eq. (23) are respectively written as (the details are given in Appendix C)

$$\begin{aligned}\int\int_{S_B^j}\left[\varphi_j^S(R_j,\Theta_j,\zeta_j)\right]_{lq}\frac{\partial G(r_j,\theta_j,z_j;R_j,\Theta_j,\zeta_j)}{\partial n_\xi}\mathrm{d}S \\ = -\int\int_{S_B^j}\frac{\partial\left[\varphi_j^I(R_j,\Theta_j,\zeta_j)\right]_{lq}}{\partial n_\xi}G(r_j,\theta_j,z_j;R_j,\Theta_j,\zeta_j)\mathrm{d}S,\end{aligned} \tag{24}$$

$$\int\int_{S_B^j}\left[\varphi_j^D(R_j,\Theta_j,\zeta_j)\right]_{lq}\frac{\partial G(r_j,\theta_j,z_j;R_j,\Theta_j,\zeta_j)}{\partial n_\xi}\mathrm{d}S = 4\pi\left[\varphi_j^I(r_j,\theta_j,z_j)\right]_{lq}, \tag{25}$$

$$\begin{aligned}\int\int_{S_B^j}\varphi_j^{R,k}(R_j,\Theta_j,\zeta_j)\frac{\partial G(r_j,\theta_j,z_j;R_j,\Theta_j,\zeta_j)}{\partial n_\xi}\mathrm{d}S \\ = \int\int_{S_B^j} n_{j,k}G(r_j,\theta_j,z_j;R_j,\Theta_j,\zeta_j)\mathrm{d}S.\end{aligned} \tag{26}$$

It should be noted that Eqs. (24), (25), and (26) must be implemented on the waterplane, i.e., the field point (r_j,θ_j,z_j) is taken from some discrete points on the interior waterplane area while the source point (R_j,Θ_j,ζ_j) locates on the immersed body surface. Since the field point and the source point can never coincide with each other, the diagonal terms associated with the solid angle coefficient vanish in Eqs. (24), (25), and (26). In addition, since the constant panel method (Liu, 2019) rather than higher-order boundary element methods is applied, evaluation of the influence between points lying on the waterline is avoided. By coupling each of these three equations with the corresponding integral equation on the immersed body surface, the 'irregular frequencies' can be effectively removed.

2.7. Other numerical aspects of the modeling

Computation of the DTM and RC can be facilitated, taking advantage of the notation in Eq. (8). Simultaneously, denoting $(\varphi_j^C)_{nm}$ as the following functions of a mode pair (n,m)

$$\left(\varphi_j^C\right)_{0m} = \frac{\cosh k(\zeta_j+h)}{\cosh kh}J_m(kR_j)\mathrm{e}^{-\mathrm{i}m\Theta_j} \quad \text{with} \quad n=0, \tag{27}$$

$$\left(\varphi_j^C\right)_{nm} = \cos k_n(\zeta_j+h)I_m(k_nR_j)\mathrm{e}^{-\mathrm{i}m\Theta_j} \quad \text{with} \quad n\geq 1, \tag{28}$$

and hence Eqs. (12) and (13) can be rearranged as

$$D_{nm}^{j,lq} = P_n\int\int_{S_B^j}\left[\left(\varphi_j^S\right)_{lq}\frac{\partial\left(\varphi_j^C\right)_{nm}}{\partial n} + \left(\varphi_j^C\right)_{nm}\frac{\partial\left(\varphi_j^I\right)_{lq}}{\partial n}\right]\mathrm{d}S, \quad \text{with} \quad n,l\in Z^* \quad \text{and} \quad m,q\in Z, \tag{29}$$

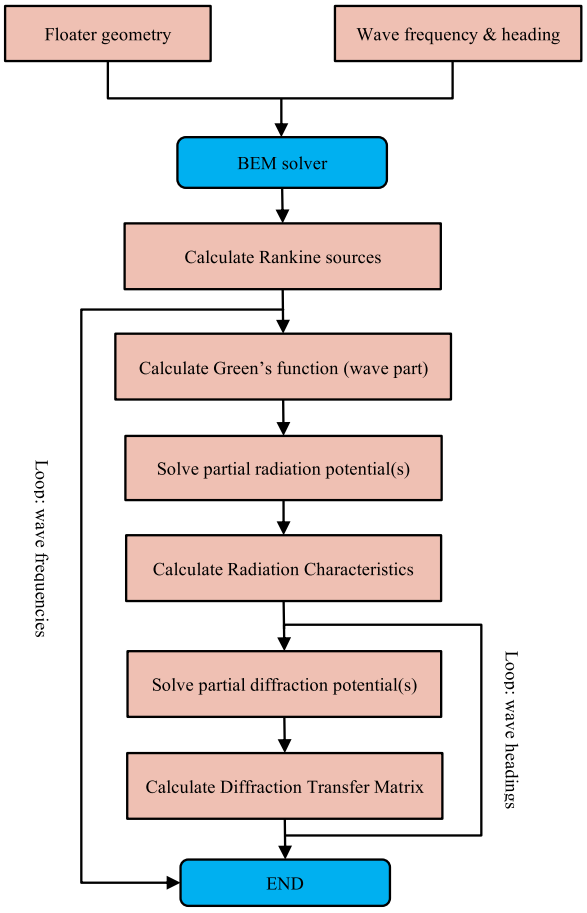

Fig. 1. Flow chart of the computation process of DTM and RC.

where Z^* represents positive integers and Z represents integers, the coefficient P_n is written as

$$P_n = \begin{cases} -\frac{\mathrm{i}}{2} C_0 \cosh^2 kh & n = 0, \\ -\frac{1}{\pi} C_n & n \geq 1. \end{cases} \tag{30}$$

Similarly, Eqs. (17) and (18) can be rearranged as

$$D_{nm}^{j,lq} = P_n \iint_{S_B^j} \left[\left(\varphi_j^S\right)_{lq} + \left(\varphi_j^I\right)_{lq} \right] \frac{\partial \left(\varphi_j^C\right)_{nm}}{\partial n} \mathrm{d}S, \text{ with } n,l \in Z^* \text{ and } m,q \in Z, \tag{31}$$

and Eqs. (21) and (22) can be rearranged as

$$R_{nm}^{j,lq} = P_n \iint_{S_B^j} \left[\varphi_j^{R,k} \frac{\partial \left(\varphi_j^C\right)_{nm}}{\partial n} - \left(\varphi_j^C\right)_{nm} n_{j,k} \right] \mathrm{d}S, \text{ with } n \in Z^* \text{ and } m \in Z. \tag{32}$$

One should take care that $(\varphi_j^C)_{nm}$ differs from $(\varphi_j^I)_{lq}$ in the sign of the power of the exponential function. Besides, since $m, q \in Z$, in order to calculate the Bessel functions with a negative integral order, the following relations can be applied (Abramowitz and Stegun, 1964)

$$J_{-m}(\mathscr{Z}) = (-1)^m J_m(\mathscr{Z}), \tag{33}$$

$$I_{-m}(\mathscr{Z}) = I_m(\mathscr{Z}), \tag{34}$$

in which $\mathscr{Z}$ is on the complex plane. Moreover, denoting a partial cylindrical wave function as f, the following equation can be used to evaluate its normal derivative

$$\frac{\partial f}{\partial n} = \left(\frac{\partial f}{\partial R} \cos\Theta - \frac{\partial f}{\partial \Theta} \frac{\sin\Theta}{R} \right) n_\xi + \left(\frac{\partial f}{\partial R} \sin\Theta + \frac{\partial f}{\partial \Theta} \frac{\cos\Theta}{R} \right) n_\eta + \frac{\partial f}{\partial \zeta} n_\zeta. \tag{35}$$

The detailed derivation of Eq. (35) can be found in Appendix D.

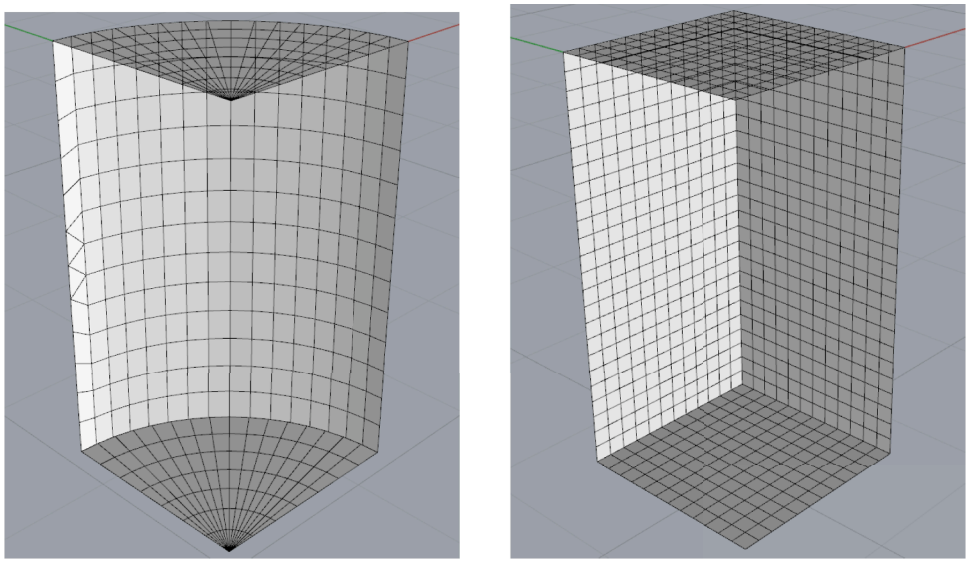

(a) (b)

Fig. 2. Mesh grids of the verifications: (a) circular cross-section cylinder; (b) square cross-section cylinder.

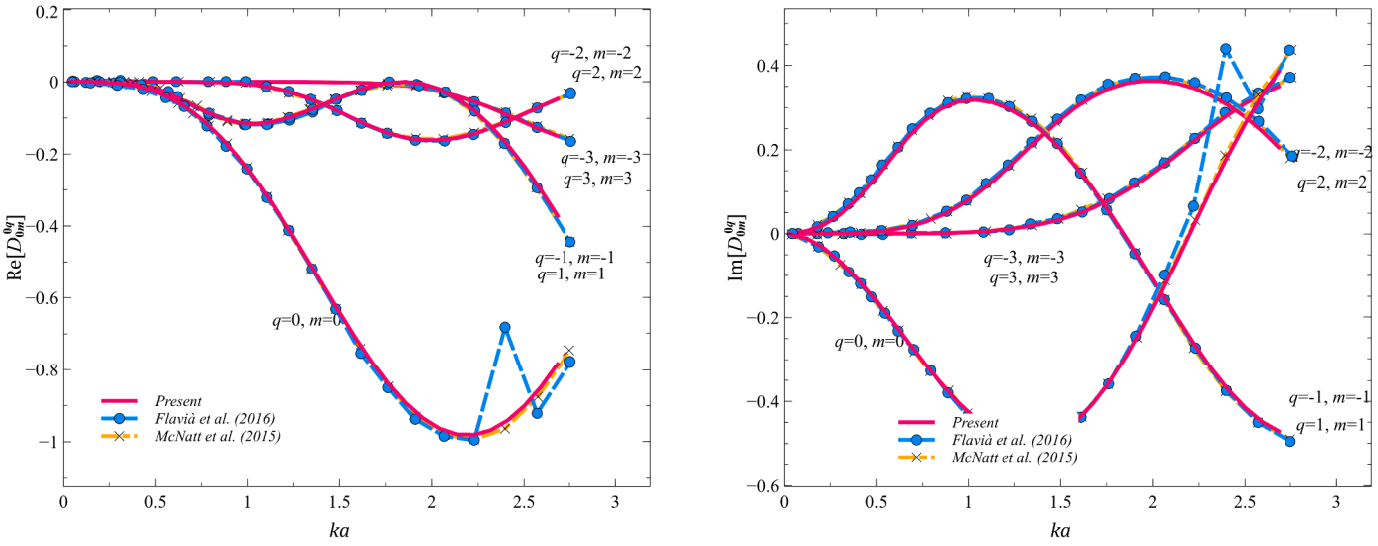

Fig. 3. DTM progressive terms for a circular cylinder of 3 m radius, 6 m draft in a 10 m water depth: (a) real part; (b) imaginary part.

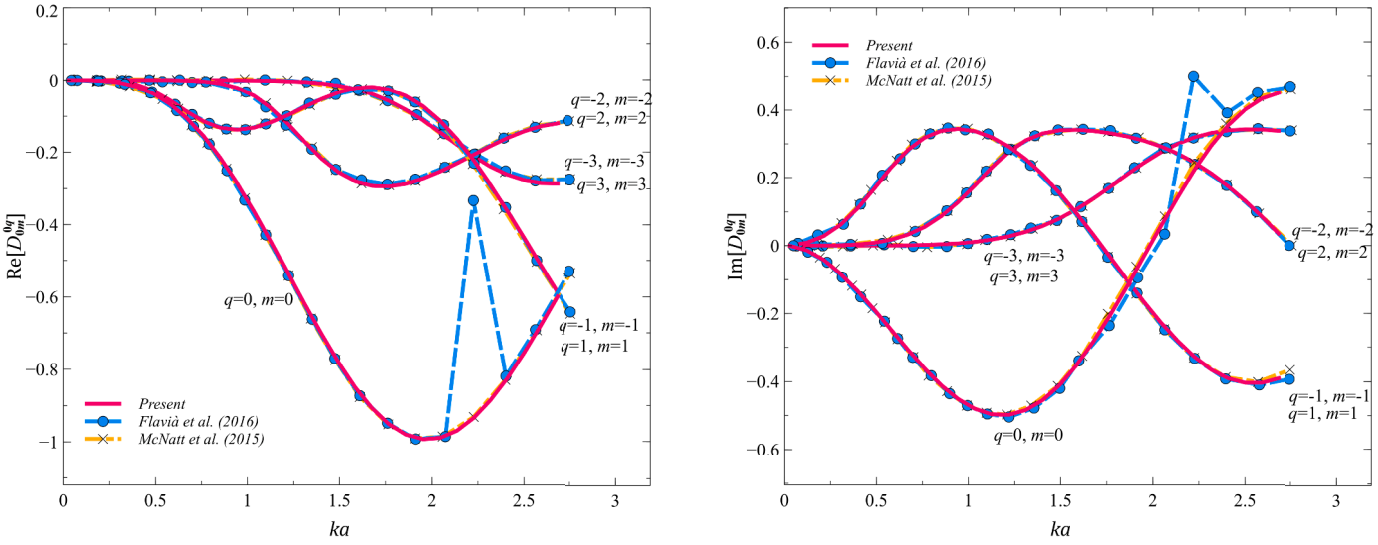

Fig. 4. DTM progressive terms for a cube box of 6 m side, 6 m draft in a 10 m water depth: (a) real part; (b) imaginary part.

3. The computation process

Computation of the DTM and the RC can be implemented based on a BEM solver (e.g., Liu et al., 2018; Liu, 2019). The computation process is illustrated in Fig. 1. Given the floater geometry and the wave frequencies & headings, the computation can be finalized via two loops. One loop is associated with the wave frequencies, and the other is related to the wave headings. The first loop solves radiation problems in which the body boundary conditions are expressed by the body surface normal vectors, as defined by Eq. (23). The second loop solves diffraction problems corresponding to a set of partial incident wave potentials, as defined by Eq. (11) or Eq. (15). In solving each radiation or diffraction problem, the left-hand side matrix and the right-hand side matrix of the linear algebraic system are assembled separately. Note that the left-hand side matrix needs to be constructed only once for all the radiation and diffraction problems at each wave frequency since it is always the same as long as the wave frequency does not change. The calculation of Green's function can be further decomposed into calculations of the Rankine part and the wave part. The former can be done prior to the two computational loops since it is completely frequency-independent, which can save a fairly large portion of computation time.

4. Results and discussions

4.1. Verification of the present method

In order to verify the present method based on the hybrid source-dipole boundary integral equation, numerical computations are performed against two benchmark problems given in Flavià et al. (2016) and Flavià et al. (2018) (the former giving more details of the computation). The two geometries are a floating truncated circular cylinder and a floating square cylinder as illustrated in Fig. 2, which are common elements in ocean renewable energy applications. The circular cylinder has a dimension of 3 m radius and 6 m draft, in the water of 10m depth.

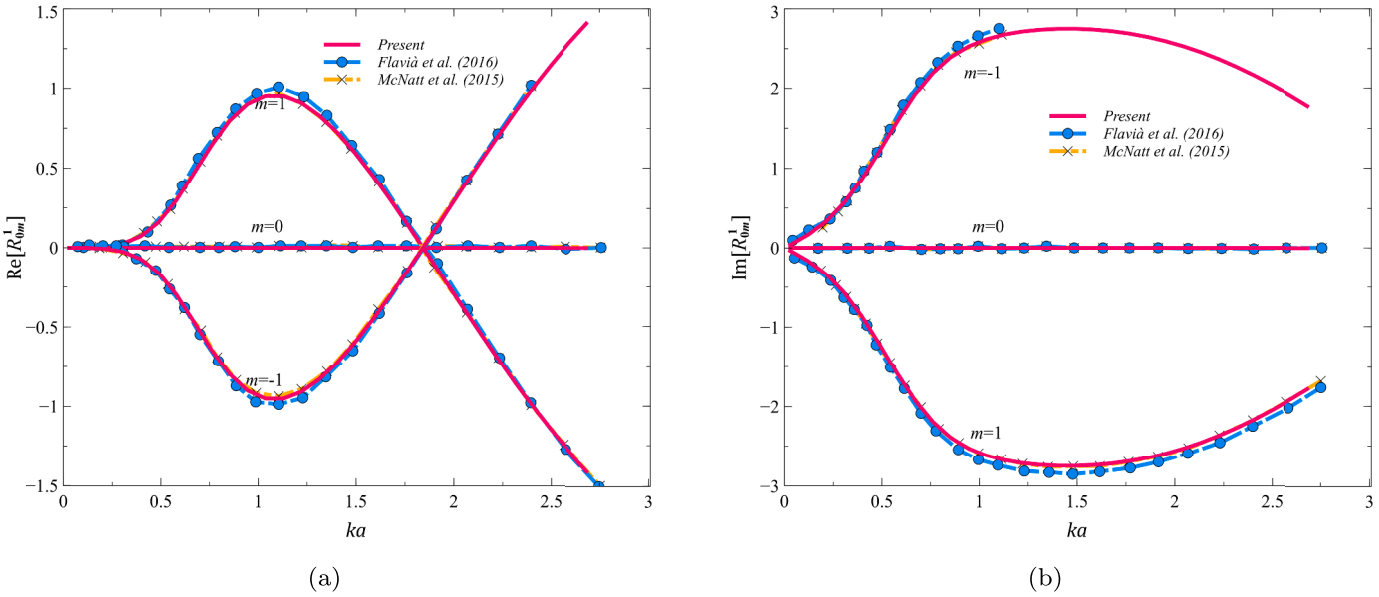

Fig. 5. RC progressive terms for a circular cylinder of 3 m radius, 6 m draft moving in surge in a 10 m water depth: (a) real part; (b) imaginary part.

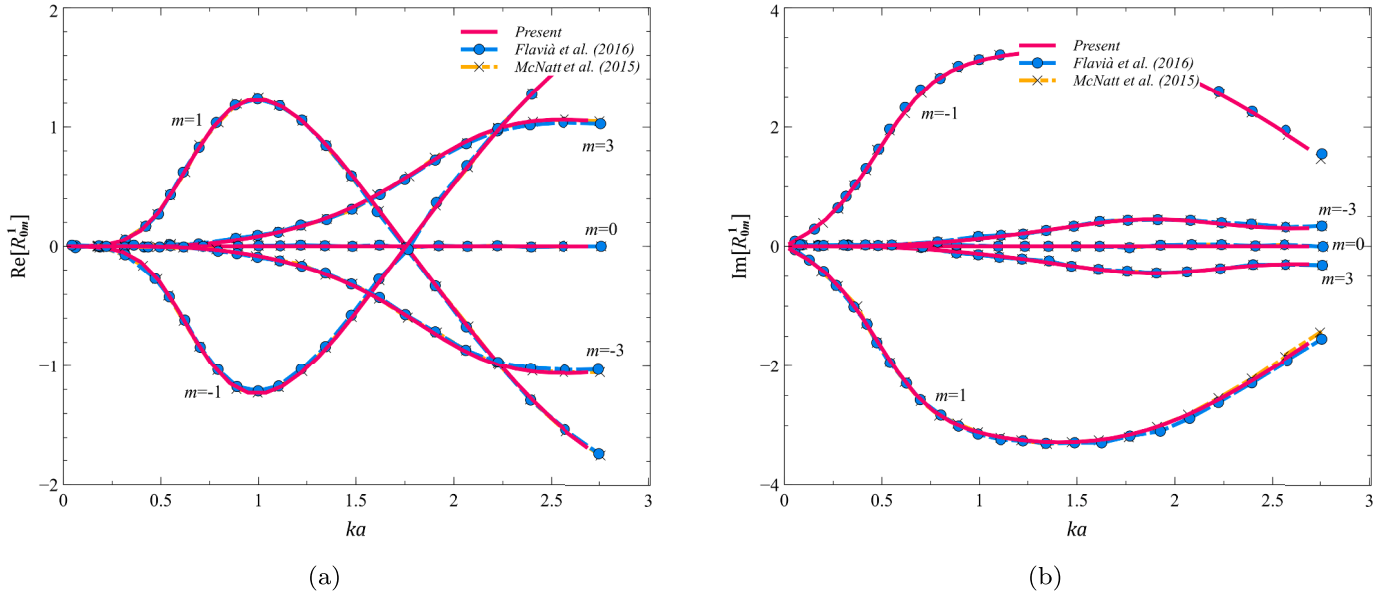

Fig. 6. RC progressive terms for a cube box of 6 m side, 6 m draft moving in surge in a 10 m water depth: (a) real part; (b) imaginary part.

One-quarter of it is meshed by 322 constant panels on the submerged body surface and 128 panels on the waterplane. The square cylinder has a side length of 6 m and 6 m draft, in the water of 10 m depth. One-quarter of it is meshed by 720 panels on the submerged body surface and 144 panels on the waterplane. It is possible that the discrete points on the interior waterplane area can be fewer, according to the study of Liang et al. (2020). In Figs. 3 – 8, 'Present' stands for the numerical results generated using 'Method I', as the results determined by 'Method I' and 'Method II' are indistinguishable. The accuracy of the two methods will be further discussed in Section 4.2.

The real and imaginary parts of the DTM terms of the two geometries are shown in Figs. 3 and 4. The numerical results of McNatt et al. (2015) and Flavià et al. (2016) are also given as a comparison. For brevity, only progressive ($n = 0, l = 0$) and non-negligible diagonal terms ($q = m$) are shown with their respective (q, m) indexes annotated. In general, a good agreement is found between results computed by the methods of McNatt et al. (2015) and Flavià et al. (2016), respectively. Exceptions occur with Flavià et al. (2016) at some specific frequencies, e.g., $ka = 2.39, 2.57, 2.75$ for the circular cylinder and $ka = 2.22, 2.40, 2.56$ for the square cylinder. This should be attributed to the 'irregular frequencies' phenomenon, as Flavià et al. (2016) was using the open-source BEM code Nemoh (Babarit and Delhommeau, 2015), which at that time did not have the 'irregular frequencies removal' functionality (Penalba et al., 2017). Nevertheless, the agreement between the present results and those of McNatt et al. (2015) is pretty good with respect to all the frequencies, as the latter was using WAMIT (Lee, 1995) with the 'irregular frequencies' being removed. In addition, it is found that the requisite number of DTM terms for the expansion in Eq. (10) depends on both the

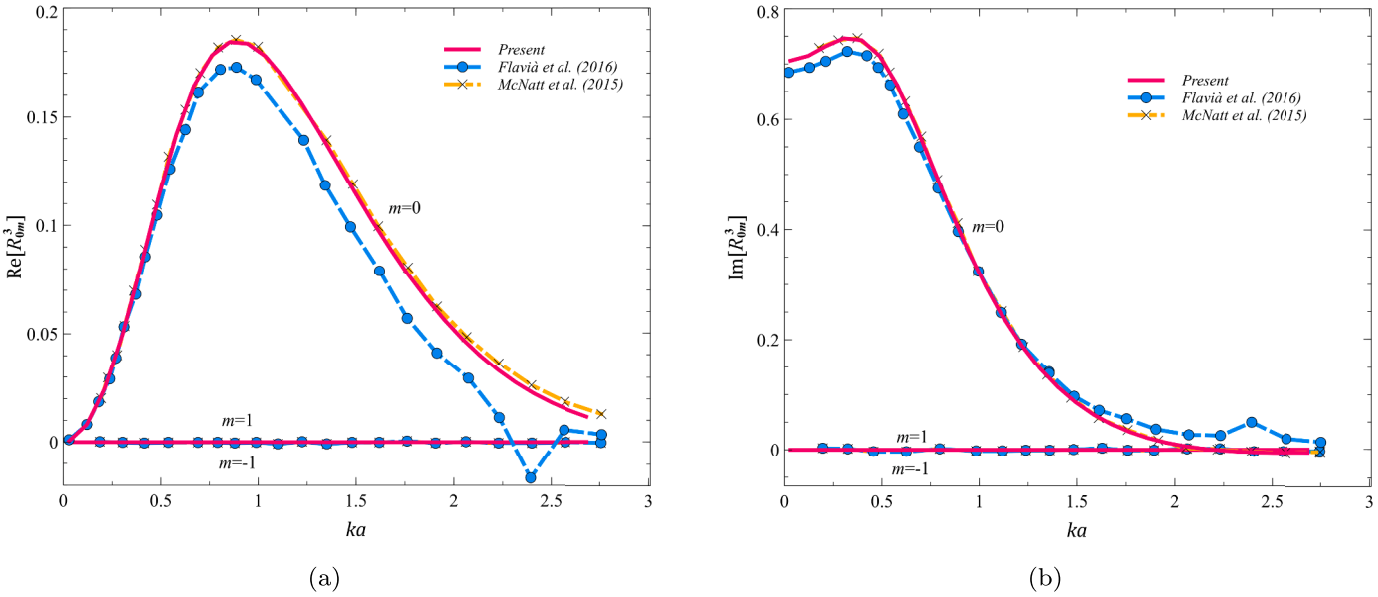

Fig. 7. RC progressive terms for a circular cylinder of 3 m radius, 6 m draft moving in heave in a 10 m water depth: (a) real part; (b) imaginary part.

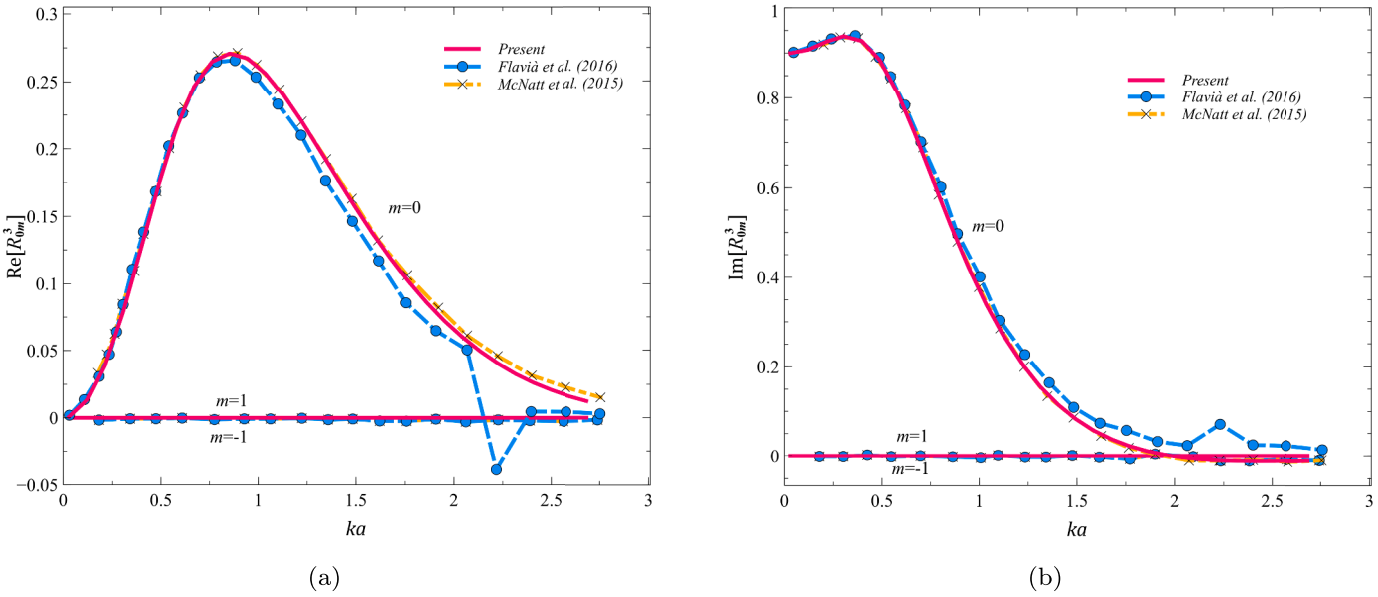

Fig. 8. RC progressive terms for a cube box of 6 m side, 6 m draft moving in heave in a 10 m water depth: (a) real part; (b) imaginary part.

geometry and the frequency. The square cylinder with fewer symmetries needs more DTM terms to finalize the series expansion of a diffraction potential.

The real and imaginary parts of the RC terms of the two geometries are shown in Figs. 5 and 6 for the surge motion and Figs. 7 and 8 for the heave motion. As to the surge motion, it is found that there are some slight discrepancies with the results of Flavià et al. (2016) regarding the circular cylinder in Fig. 5. Whereas, as to the heave motion, the discrepancies with Flavià et al. (2016) are not negligible. In addition to the abnormal places at 'irregular frequencies' as previously mentioned, there are appreciable differences between the present method with Flavià et al. (2016) in the frequency band of 0.75–2.70 rad/s, which may be attributed to the indirect BEM being used by Nemoh (Flavià et al., 2016). Nevertheless, the agreement between the present results and those of McNatt et al. (2015) is again rather good with respect to all the frequencies, as that in DTM terms. Besides, it is noted that only one mode ($m = 0$) is necessary for heave motion representing an isotropic wave (McNatt et al., 2013) while more terms are nonzero for surge motion. This is due to the high degree of symmetry when a body with at least two planes of symmetry undergoing an axisymmetric heave oscillating motion, and that the degree of symmetry reduces in the asymmetric surge motion.

4.2. Removal of irregular frequencies and the condition number

Fig. 9 gives an example of the effect of irregular frequencies, showing a comparison of the first diagonal term of DTM, i.e., D^{00}_{00}, calculated before and after the removal of irregular frequencies using the method described in Section 2.6. It is found that the irregular frequencies affect the numerical result of the DTM term in the entire frequency band. Whilst the 'true solution' behaves like sinusoidal, the 'fake solution' seems a sum of sinusoidal relations against *ka*, and its peak values are of

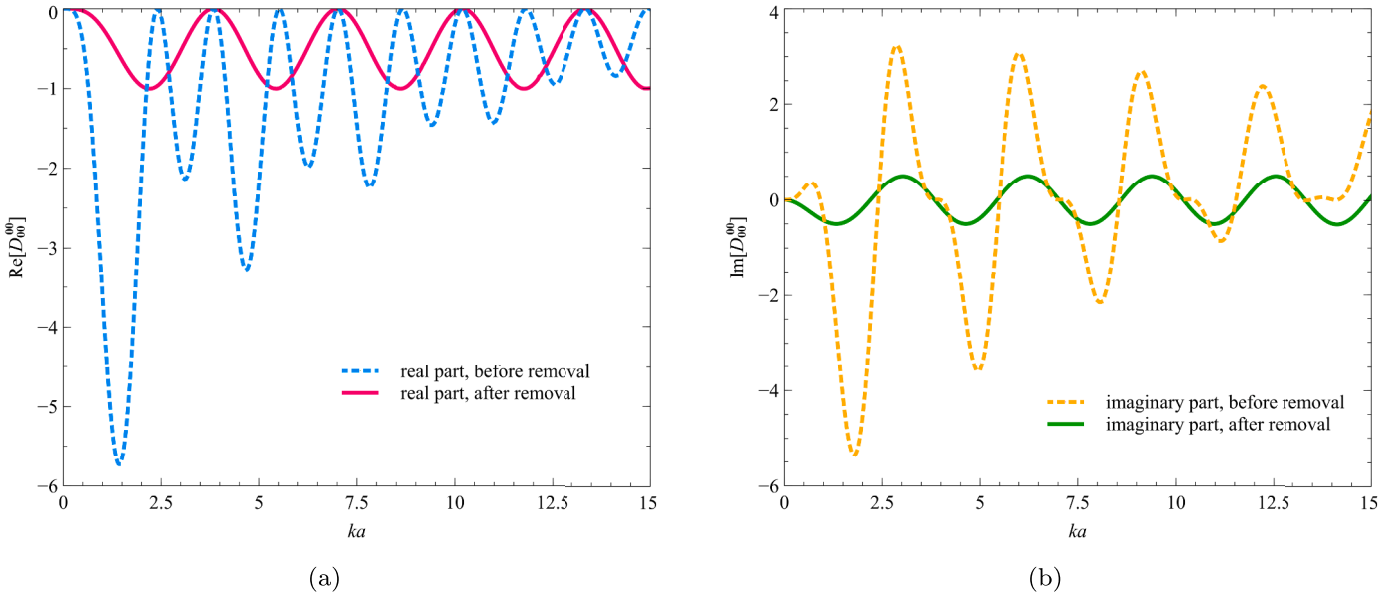

Fig. 9. Comparison of the first diagonal term of DTM of the circular cylinder calculated before and after the removal of irregular frequencies: (a) the real part; (b) the imaginary part.

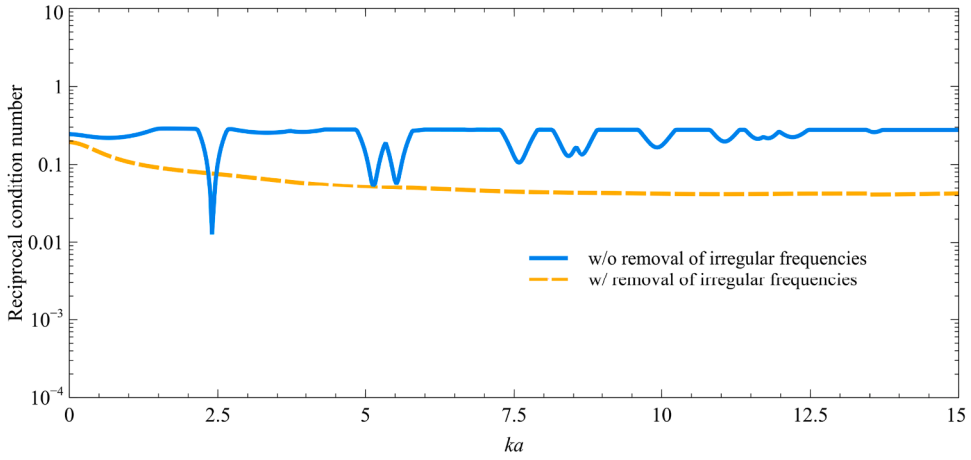

Fig. 10. Reciprocal condition number of a left-hand side sub-matrix of the circular cylinder before and after the removal of irregular frequencies.

a larger order of magnitude. Fig. 10 gives the reason for the effect of irregular frequencies, showing the reciprocal condition number of a left-hand side sub-matrix of Eqs. (14), (15), and (23). Downward spikes can be witnessed in the result without the removal of irregular frequencies, indicating large condition numbers at some frequencies where the coefficient matrix is difficult to be solved numerically. By applying the method in Section 2.6, the resultant relation of the reciprocal condition number against ka becomes rather smooth over these irregular frequencies indicating that they have been effectively removed.

To check the effect of irregular frequencies on wave forces, the interaction theory is applied to an array of four circular cylinders (Siddorn and Taylor, 2008). Excitation forces on each of the cylinders are calculated, as shown in Fig. 11. It is found that while the results of the irregular frequencies being removed match with those from the direct boundary element method, the results without removing the irregular frequencies differ much from the other two. Indeed, several large peaks can be found (e.g., $ka = 0.747$ and $ka = 1.179$ in Fig. 11) that are similar to the traditional irregular frequencies phenomenon. In addition to that, without adding any constraint on the waterplane, results (without removing the irregular frequencies) at other frequencies are neither accurate, as indicated in the calculation of DTM. This illustrates that removing the irregular frequencies is particularly important in the present method for the calculation of multiple surface-piercing bodies.

4.3. Comparison of the computational accuracy between 'method I' and 'method II'

The difference of numerical results between the two methods in the computation of the DTM of the circular cylinder is compared in Table 1 – 3. For brevity, the first two diagonal terms with $q = 0, m = 0$ and $q = 1, m = 1$ (i.e., D_{00}^{00} and D_{01}^{01}) are compared since they are the largest terms of the DTM, according to Fig. 3. The real parts and the imaginary parts are given separately in Table 1 – 3. The relative errors are calculated using the results of Method II as the base. In addition to the mesh (Mesh 1) in Fig. 2(a), a denser mesh with 617 panels (Mesh 2) over the immersed cylinder surface is used as well to check the dependency of the difference

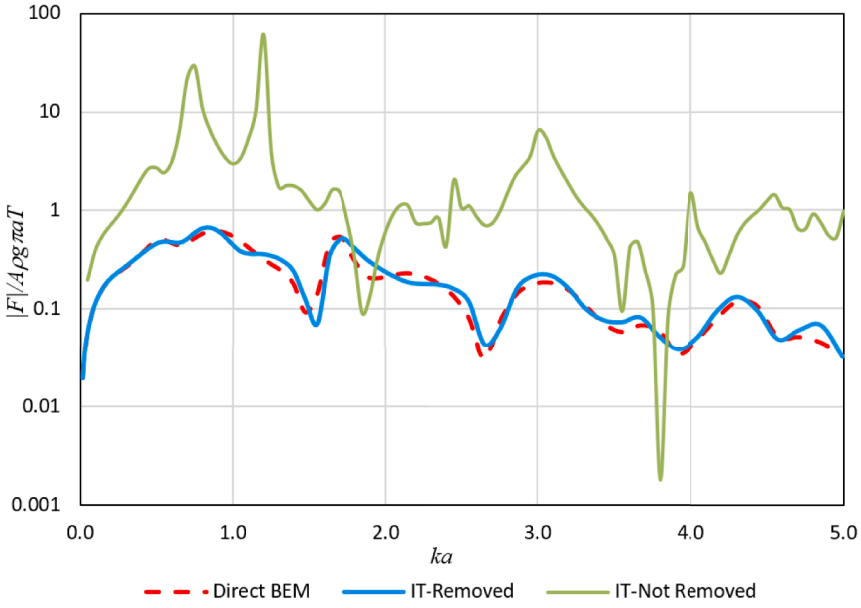

Fig. 11. Surge excitation force on Cylinder 1 of an array of 4 truncated vertical cylinders with radius a, draught $T = 2a$, in a water depth of $h = 4a$ with neighboring cylinders separated bv a distance of $4a$ for an incident wave heading angle of $\beta = \pi/4$.

on the mesh density.

It is found that, in general, the absolute values of the results of Method I are less than those of Method II. The absolute value of the relative error between the two methods increases with the increase of the wave number ka but is still acceptable around $ka = 3.0$ ($\omega = 3.132$ rad/s). As it is known that the upper limit (at which the spectrum approaches zero) of a typical wave spectrum can normally be below $\omega = 2.5$ rad/s, a small relative error of the DTM terms means that using either of the two methods can be fine for the calculation. Besides, it is found that the wave heading does not influence the DTM terms since the

Table 1
Computation based on Mesh 1 of the cylinder, in 0 ° heading waves.

	Re $q = 0, m = 0$			Im $q = 0, m = 0$			Re $q = 1, m = 1$			Im $q = 1, m = 1$		
ka	Method I	Method II	Error	Method I	Method II	Error	Method I	Method II	Error	Method I	Method II	Error
0.6	−0.04962	−0.04970	−0.16%	−0.21695	−0.21735	−0.18%	−0.03837	−0.03847	−0.28%	0.19179	0.19244	−0.34%
1.2	−0.38950	−0.39203	−0.65%	−0.48501	−0.48828	−0.67%	−0.10278	−0.10371	−0.90%	0.30207	0.30505	−0.98%
1.8	−0.85964	−0.87068	−1.27%	−0.33147	−0.33583	−1.30%	−0.00085	−0.00086	−1.14%	0.028881	0.029438	−1.89%
2.4	−0.94447	−0.96528	−2.16%	0.17974	0.18373	−2.17%	−0.16808	−0.17278	−2.72%	−0.36769	−0.37817	−2.77%
3.0	−0.50805	−0.52609	−3.43%	0.4822	0.49947	−3.46%	−0.63456	−0.65919	−3.74%	−0.45638	−0.47438	−3.79%

Table 2
Computation based on Mesh 1 of the cylinder, in 90 ° heading waves.

	Re $q = 0, m = 0$			Im $q = 0, m = 0$			Re $q = 1, m = 1$			Im $q = 1, m = 1$		
ka	Method I	Method II	Error	Method I	Method II	Error	Method I	Method II	Error	Method I	Method II	Error
0.6	−0.04962	−0.04970	−0.16%	−0.21695	−0.21735	−0.18%	−0.03837	−0.03847	−0.28%	0.19179	0.19244	−0.34%
1.2	−0.3895	−0.39203	−0.65%	−0.48501	−0.48828	−0.67%	−0.10278	−0.10371	−0.90%	0.30207	0.30505	−0.98%
1.8	−0.85964	−0.87068	−1.27%	−0.33147	−0.33583	−1.30%	−0.00085	−0.00086	−1.14%	0.028881	0.029438	−1.89%
2.4	−0.94447	−0.96528	−2.16%	0.17974	0.18373	−2.17%	−0.16808	−0.17278	−2.72%	−0.36769	−0.37817	−2.77%
3.0	−0.50805	−0.52609	−3.43%	0.4822	0.49947	−3.46%	−0.63456	−0.65919	−3.74%	−0.45638	−0.47438	−3.79%

Table 3
Computation based on Mesh 2 of the cylinder, in 0 ° heading waves.

	Re $q = 0, m = 0$			Im $q = 0, m = 0$			Re $q = 1, m = 1$			Im $q = 1, m = 1$		
ka	Method I	Method II	Error	Method I	Method II	Error	Method I	Method II	Error	Method I	Method II	Error
0.6	−0.04968	−0.04972	−0.06%	−0.21722	−0.21736	−0.06%	−0.03813	−0.03816	−0.08%	0.19142	0.19158	−0.08%
1.2	−0.39099	−0.39197	−0.25%	−0.48696	−0.48819	−0.25%	−0.10227	−0.10251	−0.23%	0.30260	0.30333	−0.24%
1.8	−0.86636	−0.87072	−0.50%	−0.33384	−0.33553	−0.50%	−0.00082	−0.00082	−0.49%	0.028486	0.028642	−0.54%
2.4	−0.95666	−0.96453	−0.82%	0.18351	0.18502	−0.82%	−0.17048	−0.17212	−0.95%	−0.37388	−0.37750	−0.96%
3.0	−0.51702	−0.52365	−1.27%	0.49312	0.49945	−1.27%	−0.6481	−0.65744	−1.42%	−0.46784	−0.47460	−1.42%

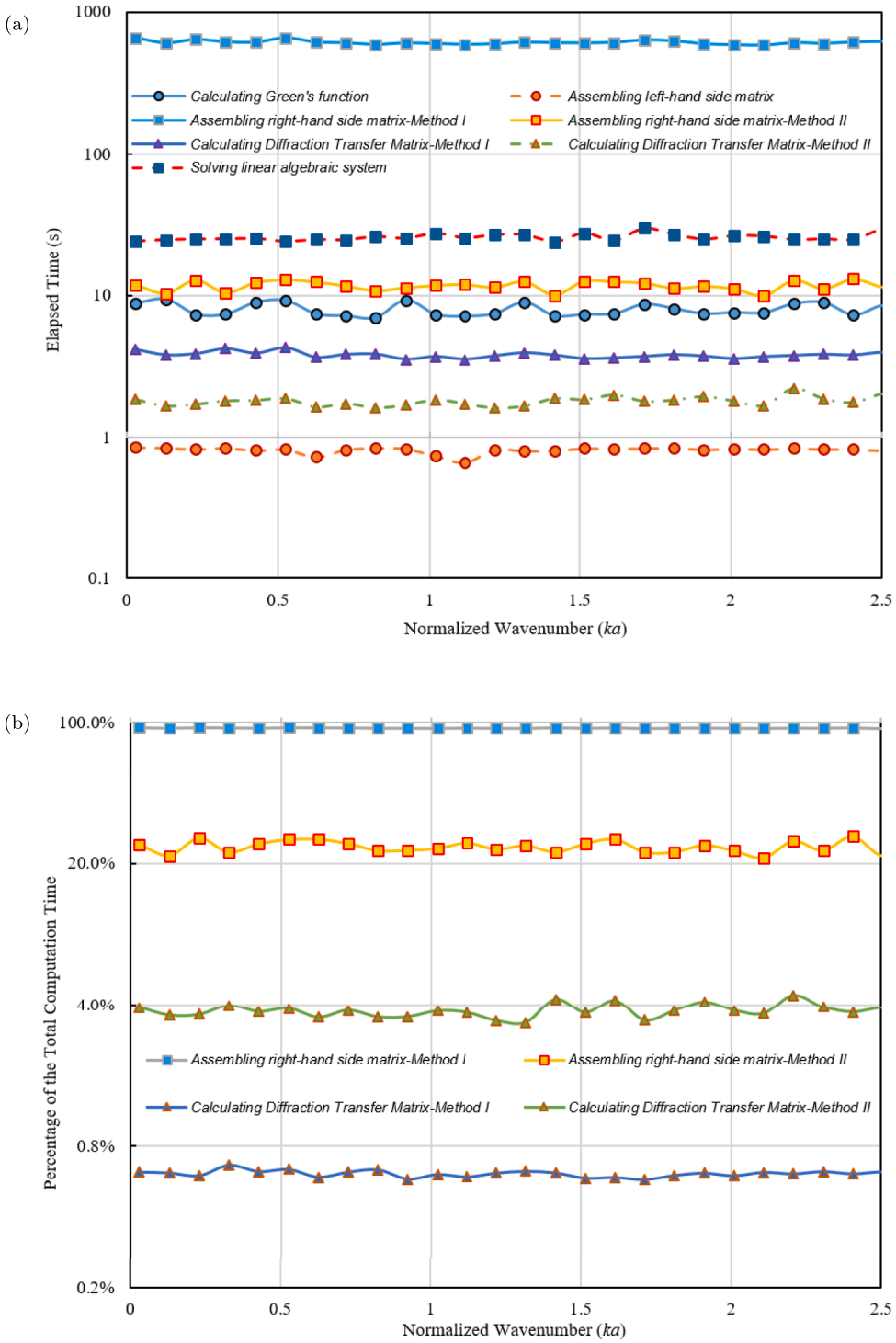

Fig. 12. Time cost of per-frequency computation for the diffraction problem: (a) the elasped computation time, (b) the percentages of the time cost in the entire computation process using two different methods.

partial wave components (Eqs. (8) and (9)) do not involve the wave heading information. Furthermore, it is reasonable that the two methods have some minor differences. The difference comes from the different imposing conditions at the right-hand side of the boundary integral equation, say, Eqs. (14) and (15). Since in Method II the right-hand side is simply a wave incident potential at a single field point, while in Method I, it is a complex surface integral of the product of the derivatives of incident potential and Greens function, Method II is expected to be more accurate than Method I. In other words, the accuracy of Method I depends more heavily on the geometrical discretization (because of the surface integral in Eq. (14) over the body). Therefore, when using Method I, the mesh needs to be denser in the higher frequency region than in the lower frequency region to achieve equivalent accuracy in both regions. However, for Method II, this restriction is weaker than Method I. Nevertheless, increasing the mesh density can reduce the difference between the two methods, as shown in Table 1 and 3.

Table 4
Increase of the time cost of per-frequency (e.g., $ka = 0.921$) DTM computation against the maximum truncation mode: the 2nd and 3rd columns give the total CPU times using Method I and II; the rest 4th–7th columns give the percentage of the time cost in the total CPU times at different stages using the two methods.

l_{Max}, q_{Max}	CPU Time Method I	CPU Time Method II	Assembling right-hand side matrix Method I	Assembling right-hand side matrix Method II	Calculating DTM Method I	Calculating DTM Method II
0	23.12 (s)	12.31 (s)	39.53%	1.39%	15.29%	13.75%
1	70.75 (s)	15.10 (s)	77.50%	6.78%	5.00%	11.21%
2	156.48 (s)	20.12 (s)	87.60%	12.71%	2.26%	8.41%
3	280.32 (s)	27.37 (s)	91.28%	17.44%	1.26%	6.18%
4	442.26 (s)	36.85 (s)	92.99%	20.82%	0.80%	4.59%
5	642.31 (s)	48.57 (s)	93.90%	23.17%	0.55%	3.48%
10	2214.10 (s)	140.60 (s)	95.35%	28.01%	0.16%	1.20%

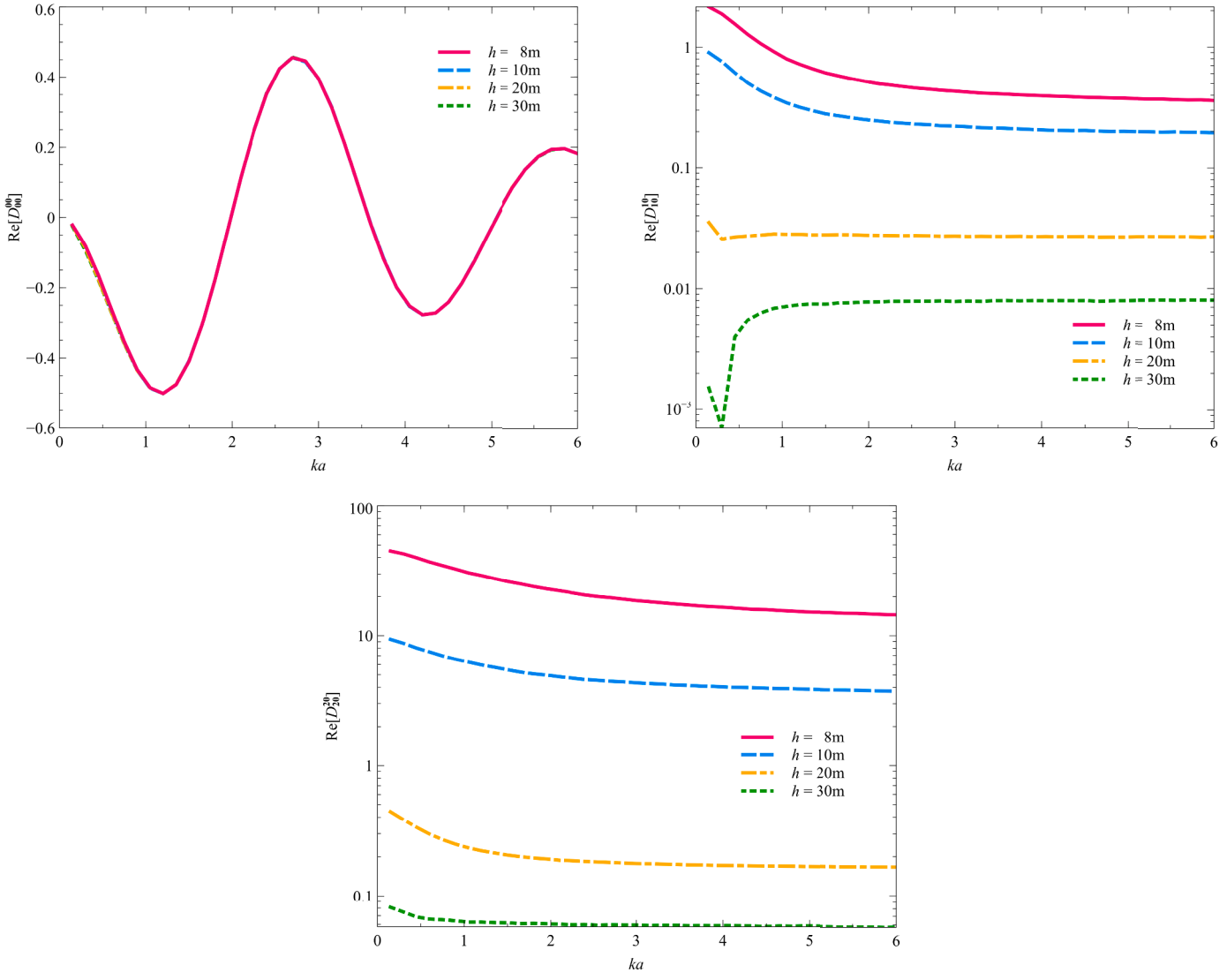

(a)

Fig. 13. Comparison of the DTM terms with $q = 0$, $m = 0$ of the cube box at different water depth: (a) $l = 0$, $n = 0$; (b) $l = 1$, $n = 1$; (c) $l = 2$, $n = 2$.

4.4. Comparison of the computational efficiency between 'method I' and 'method II'

Fig. 12 shows the CPU time (unit: s) of per evaluation of the DTM of the floating square cylinder at different stages, on a desktop machine with an Intel(R) Xeon(R) E5-2620 v3 CPU of 2.40 GHz. The computations are performed with the aid of OpenMP parallelism on eight threads of cores, and the CPU times are obtained based on wave diffraction computations with respect to 36 wave headings. Each wave diffraction computation consists of five stages. In order to show clearly the differences, the logarithmic scale is used for the 'Elasped Time'-axis. In Fig. 12, Eq. (10) has been truncated with a maximum depth mode of

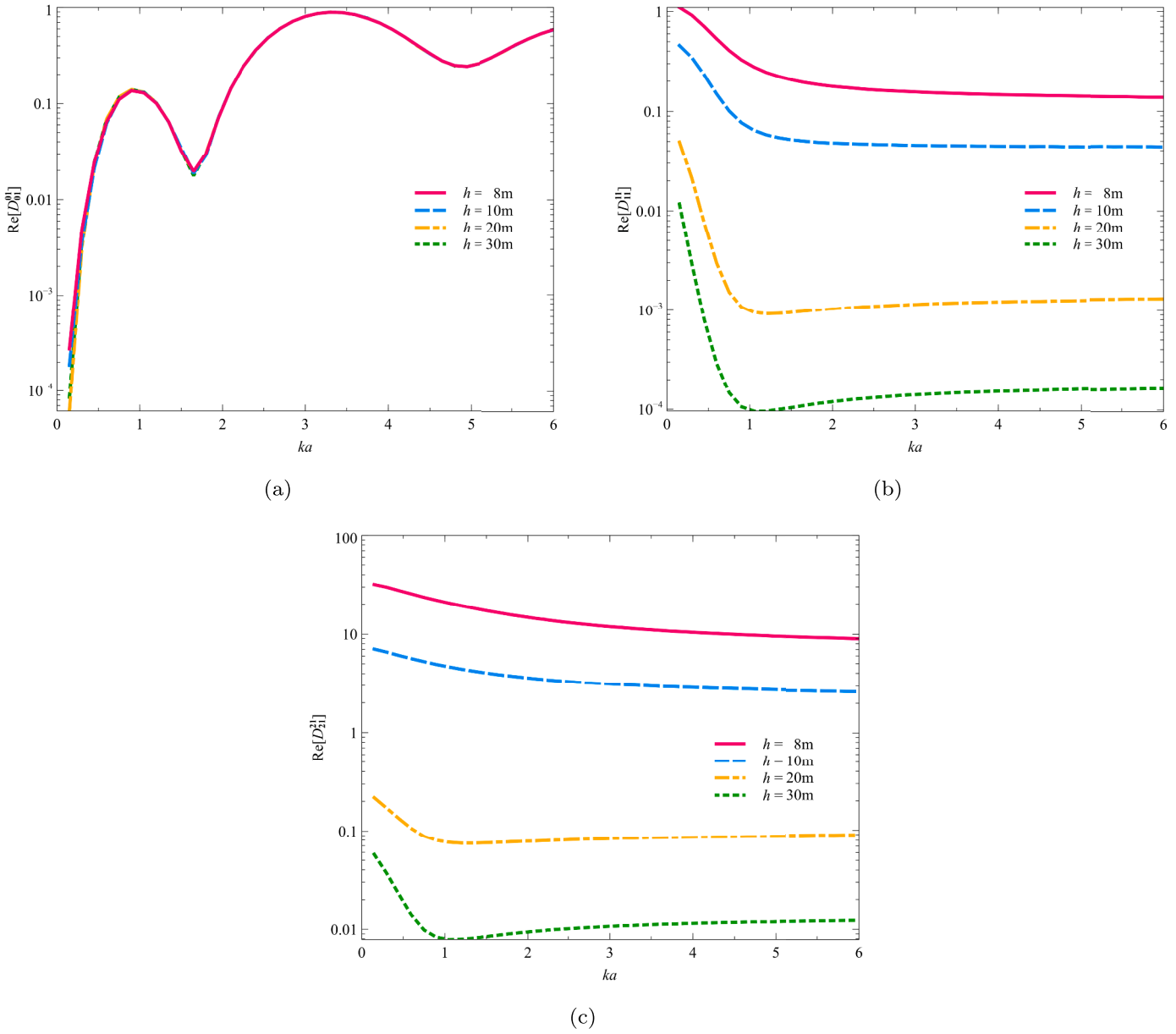

Fig. 14. Comparison of the DTM terms with $q = 1$, $m = 1$ of the cube box at different water depth: (a) $l = 0$, $n = 0$; (b) $l = 1$, $n = 1$; (c) $l = 2$, $n = 2$.

$N_{\text{Max}} = 5$ and a maximum angular mode of $M_{\text{Max}} = 5$, which means that the number of diffraction problems to be solved at each frequency is $(N_{\text{Max}}+1)(2M_{\text{Max}}+1)N_{\text{WaveHeadings}} = 2376$ and the number of the diffraction transfer matrices to be calculated is $N_{\text{WaveHeadings}} = 36$. It is found that assembling the right-hand side matrix takes up most of the time (93.90% of the overall computation time) in Method I, while solving the linear algebraic system costs the most in Method II. Note that herein 'assembling the right-hand side matrix' involves the calculation of the right-hand side of Eq. (14) or Eq. (15), as well as the construction of the right-hand side of the overdetermined integral equations encountered in the least-squares problem (Liu, 2019; Liang et al., 2020). Furthermore results regarding the time cost at a certain frequency are given in Table 4. It is found that the total CPU time and the percentage of 'assembling the right-hand side matrix' increase rapidly in Method I with respect to the truncation mode (for brevity $N_{\text{Max}} = M_{\text{Max}}$ is taken here, but it is not always necessarily). While the total CPU time of Method I is twice that of Method II when $N_{\text{Max}} = 0$, it increases significantly to 15.75 times that of Method II when $N_{\text{Max}} = 10$. It is worth mentioning that for Method I, the percentage of 'assembling the right-hand side matrix' quickly increases to above 90% as the truncation mode increases merely to 3. Both of these results show that, Method I is much more computationally expensive due to the more complex right-hand side of the boundary integral equation (i.e., Eq. (1)). On the other hand, 'calculating Diffraction Transfer Matrix' seems to have occupied a much smaller portion of the computational resource in contrast to the largest part, regardless of which method is being used.

4.5. Water-depth dependance of the diffraction transfer matrix

The DTM and RC are dependent on the water depth. Herein, we take DTM of the cube box for example. Fig. 13 and Fig. 14 show respectively the real part of its DTM terms of $q = 0$, $m = 0$ and $q = 1$, $m = 1$ at different water depth. It is found that for the first term (when the depth mode l of the partial incident waves and n of the outgoing waves are both

zero), the value of DTM terms has little dependance on the water depth h, while the value of the rest DTM terms decreases substantially with the increase of h. This can be explained from Eq. (4), Eq. (5) and Eqs. (27) – (30). Whereas the terms $(\varphi_j^I)_{lq}$, $(\varphi_j^S)_{lq}$ and $(\varphi_j^C)_{nm}$ inside the integration are almost independent of h from the definitions, a straightforward asymptotic analysis can give the dominant order of the expansion coefficient P_n:

$$P_n = \begin{cases} -\frac{\mathrm{i}}{2}k & n = 0, \\ -\frac{1}{\pi h} & n \geq 1. \end{cases} \tag{36}$$

Eq. (36) illustrates mathematically that the DTM terms of $n \geq 1$ are inversely proportional to h while the first term of $n = 0$ is independent of h. In addition, it is noted that this inversely proportional relationship still holds in case if the normalization is taken as well for the evanescent modes as for the propagating mode in Eqs. (8) and (9).

5. Conclusions

An alternative method of evaluating the DTM and the RC encountered in wave interactions with multiple bodies is presented. The complete derivation process and the resultant mathematical formulations are given in detail. Good agreement is achieved with the conventional source-distribution-based method, which has been used by Goo and Yoshida (1990) and Flavià et al. (2018), etc. The irregular frequencies are removed by the overdetermined integral equations proposed firstly by Ohmatsu (1983) and summarized recently in Liang et al. (2020). Two alternative ways of computing the DTM are compared, i.e., one integrates the distributions of the normal derivative of partial incident wave potentials over the submerged body surface, and the other simply evaluates the partial incident wave potentials at a field point as firstly applied by Kashiwagi (2000). The comparative study shows that while the accuracy of the two approaches does not differ much, the computation cost can be substantially saved using the latter approach. Moreover, it is found that when more terms of DTM need to be calculated, the increase of the truncation mode can lead to a significant increase of the overall CPU time as well as the percentage of assembling the right-hand side matrix, for which issue applying the first approach can be no longer acceptable. The present study may provide appropriate options for the subsequent researchers to choose from, especially when they are using a numerical method based on the hybrid source-dipole boundary integral equations.

Declaration of Competing Interest

The authors declare that they have no known competing financial interests or personal relationships that could have appeared to influence the work reported in this paper.

Acknowledgment

The financial support from the Grant-in-Aid for Early-Career Scientists (JSPS KAKENHI Grant Number JP18K13939) and the Open Research Fund (Grant Number LP1815) of the State Key Laboratory of Coastal and Offshore Engineering (SKLCOE) of Dalian University of Technology are gratefully acknowledged.

Appendix A. Derivation of the Green function in polar coordinates

Introducing the cylindrical coordinate transformation

$$(x, y) = r(\cos\theta, \sin\theta) \quad \text{and} \quad (\xi, \eta) = R(\cos\Theta, \sin\Theta) \tag{A.1}$$

It is noted from Fig. Appendix A.1 that $L^2 = R^2 + r^2 - 2Rr\cos(\theta - \Theta)$. Applying Graf's addition theorem (Watson, 1995), it is straightforward to obtain

$$J_0(kL) = \sum_{m=-\infty}^{\infty} J_m(kR)J_m(kr)\mathrm{e}^{\mathrm{i}m(\theta-\Theta)}, \tag{A.2}$$

$$Y_0(kL) = \sum_{m=-\infty}^{\infty} \left\{\frac{J_m(kR)Y_m(kr)}{Y_m(kR)J_m(kr)}\right\}\mathrm{e}^{\mathrm{i}m(\theta-\Theta)}, \tag{A.3}$$

$$K_0(k_nL) = \sum_{m=-\infty}^{\infty} \left\{\frac{I_m(k_nR)K_m(k_nr)}{K_m(k_nR)I_m(k_nr)}\right\}\mathrm{e}^{\mathrm{i}m(\theta-\Theta)}. \tag{A.4}$$

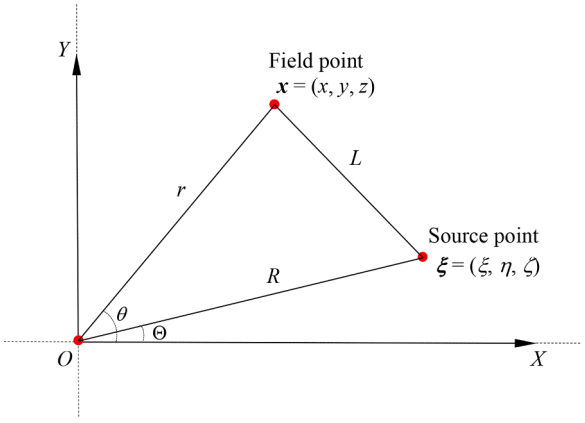

Fig. Appendix A.1. Schematic of the plane view of Graf's addition theorem and the reference system.

Considering $H_m^{(1)} = J_m + \mathrm{i}Y_m$, we can further obtain

$$H_0^{(1)}(kL) = \sum_{m=-\infty}^{\infty} \left\{ \frac{J_m(kR)H_m^{(1)}(kr)}{H_m^{(1)}(kR)J_m(kr)} \right\} \mathrm{e}^{\mathrm{i}m(\theta-\Theta)}. \tag{A.5}$$

Note that in Eqs. (Appendix A.3), (Appendix A.4) and (Appendix A.5), the upper terms in the curly braces are valid provided $r \geq R$ and the lower terms are valid provided $r < R$. In contrast, Eq. (Appendix A.2) is valid for all values of R and r. Substituting the Eqs. (Appendix A.4) and (Appendix A.5) into Eq. (3), the free-surface Green function can be expressed as a series of cylindrical harmonics, i.e.,

$$\begin{aligned} G = \; & 2\pi \mathrm{i} C_0 \cosh k(z+h)\cosh k(\zeta+h) \sum_{m=-\infty}^{\infty} \left\{ \frac{J_m(kR)H_m^{(1)}(kr)}{H_m^{(1)}(kR)J_m(kr)} \right\} \mathrm{e}^{\mathrm{i}m(\theta-\Theta)} \\ & + 4\sum_{n=1}^{\infty} C_n \cos k_n(z+h)\cos k_n(\zeta+h) \sum_{m=-\infty}^{\infty} \left\{ \frac{I_m(k_nR)K_m(k_nr)}{K_m(k_nR)I_m(k_nr)} \right\} \mathrm{e}^{\mathrm{i}m(\theta-\Theta)}, \end{aligned} \tag{A.6}$$

In essence, Eq. (Appendix A.6) transfers the influence between the field point $\boldsymbol{x}$ and the source point $\boldsymbol{\xi}$ to those respectively with respect to the origin O, as illustrated by Fig. Appendix A.1. Note that the wavenumber k is the positive root of the water wave dispersion equation

$$k\tanh kh = K, \tag{A.7}$$

and k_n ($n = 0, 1, 2\ldots$) satisfies the following equation

$$k_n \tan k_n h = -K, \tag{A.8}$$

where k_0 is imaginary, $k_0 = -\mathrm{i}k$ (i is the imaginary unit), and k_n ($n = 1, 2, \ldots$) are positive, characterizing the evanescent modes of the eigenfunction expansion.

Appendix B. Derivation of the integral equation of solving the total diffraction potential

The following derivation involves two alternative approaches. The first approach was first proposed by Lee (1995) and the detailed derivation can be found in Teng (2016). It is known to all that for the scattering potential ϕ_S, when the field point locates on the body surface, Eq. (1) reads

$$2\pi\varphi_S(\boldsymbol{x}) + \int\int S_B \varphi_S(\boldsymbol{\xi}) \frac{\partial G(\boldsymbol{x},\boldsymbol{\xi})}{\partial n_{\boldsymbol{\xi}}} \mathrm{d}S = \int\int_{S_B} G(\boldsymbol{x},\boldsymbol{\xi}) \frac{\partial \varphi_S(\boldsymbol{\xi})}{\partial n_{\boldsymbol{\xi}}} \mathrm{d}S. \tag{B.1}$$

Consider the incident potential φ_I in the presence of a body (or bodies). Because φ_I does not satisfy the far-field radiation condition, the next boundary integral equation can be constructed in the fluid domain enclosed by the body surface and a far-field control surface:

$$2\pi\varphi_I(\boldsymbol{x}) + \int\int S_B + S_\infty \varphi_I(\boldsymbol{\xi}) \frac{\partial G(\boldsymbol{x},\boldsymbol{\xi})}{\partial n_{\boldsymbol{\xi}}} \mathrm{d}S = \int\int_{S_B+S_\infty} G(\boldsymbol{x},\boldsymbol{\xi}) \frac{\partial \varphi_I(\boldsymbol{\xi})}{\partial n_{\boldsymbol{\xi}}} \mathrm{d}S. \tag{B.2}$$

In the case that there is no body in place, Eq. (Appendix B.2) becomes

$$4\pi\varphi_I(\boldsymbol{x}) + \int\int_{S_\infty} \varphi_I(\boldsymbol{\xi}) \frac{\partial G(\boldsymbol{x},\boldsymbol{\xi})}{\partial n_{\boldsymbol{\xi}}} \mathrm{d}S = \int\int_{S_\infty} G(\boldsymbol{x},\boldsymbol{\xi}) \frac{\partial \varphi_I(\boldsymbol{\xi})}{\partial n_{\boldsymbol{\xi}}} \mathrm{d}S. \tag{B.3}$$

Note that in Eq. (Appendix B.3), $C(\boldsymbol{x}) = 4\pi$, since there exists only fluid. Subtracting Eq. (Appendix B.3) from Eq. (Appendix B.2) yields

$$-2\pi\varphi_I(\boldsymbol{x}) + \int\int S_B \varphi_I(\boldsymbol{\xi}) \frac{\partial G(\boldsymbol{x},\boldsymbol{\xi})}{\partial n_{\boldsymbol{\xi}}} \mathrm{d}S = \int\int_{S_B} G(\boldsymbol{x},\boldsymbol{\xi}) \frac{\partial \varphi_I(\boldsymbol{\xi})}{\partial n_{\boldsymbol{\xi}}} \mathrm{d}S. \tag{B.4}$$

Combining Eqs. (Appendix B.1) and (Appendix B.4), we obtain

$$2\pi\varphi_D(\boldsymbol{x}) - 4\pi\varphi_I(\boldsymbol{x}) + \int\int S_B \varphi_D(\boldsymbol{\xi}) \frac{\partial G(\boldsymbol{x},\boldsymbol{\xi})}{\partial n_{\boldsymbol{\xi}}} \mathrm{d}S = \int\int_{S_B} G(\boldsymbol{x},\boldsymbol{\xi}) \frac{\partial \varphi_D(\boldsymbol{\xi})}{\partial n_{\boldsymbol{\xi}}} \mathrm{d}S, \tag{B.5}$$

where $\varphi_D(\boldsymbol{x}) = \varphi_I(\boldsymbol{x}) + \varphi_S(\boldsymbol{x})$. φ_D is termed as diffraction potential. Further, since on the immersed body boundary surface φ_D satisfies the impermeable condition, the right-hand side of Eq. (Appendix B.5) is zero. This finally leads to

$$2\pi\varphi_D(\boldsymbol{x}) + \int\int S_B \varphi_D(\boldsymbol{\xi}) \frac{\partial G(\boldsymbol{x},\boldsymbol{\xi})}{\partial n_{\boldsymbol{\xi}}} \mathrm{d}S = 4\pi\varphi_I(\boldsymbol{x}) \tag{B.6}$$

The second approach can be more straightforward. Let us consider a virtual incident wave potential inside of the body. Because the inner domain is encompassed by the body surface and the interior free surface, Eq. (Appendix B.4) can be directly obtained. This approach has been mentioned in Kashiwagi (2003). However, one should note that the 'solid angle coefficient' in this case is negative 2π, which is attributed to the normal direction as it has been defined initially outward the body surface (i.e., directing into the fluid domain). Then, a combination of Eqs. (Appendix B.1) and (Appendix B.4) gives rise to Eq. (Appendix B.6).

Appendix C. Derivation of the overdetermined integral equations

Consider a field point locating on the interior waterplane surface. The free term (associated with the 'solid angle coefficient') at the left-hand side of Eq. (Appendix B.1) vanishes due to the fact that there is no longer any Cauchy-type singularity caused by the coincidence of the field point and the source point. Thereby, we obtain an integral equation to be satisfied on the waterplane

$$\iint_{S_B} \varphi_S(\boldsymbol{\xi}) \frac{\partial G(\boldsymbol{x},\boldsymbol{\xi})}{\partial n_{\boldsymbol{\xi}}} \mathrm{d}S = \iint_{S_B} G(\boldsymbol{x},\boldsymbol{\xi}) \frac{\partial \varphi_S(\boldsymbol{\xi})}{\partial n_{\boldsymbol{\xi}}} \mathrm{d}S. \tag{C.1}$$

The combination of Eqs. (Appendix B.1) and (Appendix C.1) leads to an overdetermined system of the scattering wave potential. Worthy mentions are that Eq. (Appendix C.1) can be obtained as well by considering a degenerated form of the extended integral equations (Liang et al., 2020) as the dipole strengths over the interior waterplane surface are zero and can be neglected. Secondly, applying a similar procedure, it is straightforward to obtain from Eq. (Appendix B.6) the

$$\iint_{S_B} \varphi_D(\boldsymbol{\xi}) \frac{\partial G(\boldsymbol{x},\boldsymbol{\xi})}{\partial n_{\boldsymbol{\xi}}} \mathrm{d}S = 4\pi\varphi_I(\boldsymbol{x}), \tag{C.2}$$

is satisfied on the waterplane. The combination of Eqs. (Appendix B.6) and (Appendix C.2) leads to another overdetermined system regarding the total diffraction potential.

Alternatively, Eq. (Appendix C.2) can also be obtained by considering a virtual incident wave potential in the inner domain enclosed by the body surface and interior free surface, which reads

$$-4\pi\varphi_I(\boldsymbol{x}) + \iint_{S_B} \varphi_I(\boldsymbol{\xi}) \frac{\partial G(\boldsymbol{x},\boldsymbol{\xi})}{\partial n_{\boldsymbol{\xi}}} \mathrm{d}S = \iint_{S_B} G(\boldsymbol{x},\boldsymbol{\xi}) \frac{\partial \varphi_I(\boldsymbol{\xi})}{\partial n_{\boldsymbol{\xi}}} \mathrm{d}S. \tag{C.3}$$

The 'solid angle coefficient' -4π is due to the opposite normal direction together with the vanishing of any boundary in the neighborhood of the field point. A combination of Eq. (Appendix C.1) and Eq. (Appendix C.3) yields a supplemental integral equation free of irregular frequencies, which is precisely Eq. (Appendix C.2).

Appendix D. Derivation of the normal derivative of a cylindrical function

Denote f to be a function of the polar coordinates (R,Θ,ζ), it is straightforward to derive the following relationship

$$\frac{\partial f}{\partial n} = \frac{\partial f}{\partial \xi}\frac{\partial \xi}{\partial n} + \frac{\partial f}{\partial \eta}\frac{\partial \eta}{\partial n} + \frac{\partial f}{\partial \zeta}\frac{\partial \zeta}{\partial n} = \frac{\partial f}{\partial \xi}n_\xi + \frac{\partial f}{\partial \eta}n_\eta + \frac{\partial f}{\partial \zeta}n_\zeta, \tag{C.1}$$

$$\frac{\partial f}{\partial \xi} = \frac{\partial f}{\partial R}\frac{\partial R}{\partial \xi} + \frac{\partial f}{\partial \Theta}\frac{\partial \Theta}{\partial \xi} = \frac{\partial f}{\partial R}\cos\Theta - \frac{\partial f}{\partial \Theta}\frac{\sin\Theta}{R}, \tag{C.2}$$

$$\frac{\partial f}{\partial \eta} = \frac{\partial f}{\partial R}\frac{\partial R}{\partial \eta} + \frac{\partial f}{\partial \Theta}\frac{\partial \Theta}{\partial \eta} = \frac{\partial f}{\partial R}\sin\Theta + \frac{\partial f}{\partial \Theta}\frac{\cos\Theta}{R}, \tag{C.3}$$

where $\boldsymbol{n} = (n_\xi, n_\eta, n_\zeta)$ is the normal derivative of a panel centered at a source point $\boldsymbol{\xi} = (\xi,\eta,\zeta) = (R\cos\Theta, R\sin\Theta, \zeta)$. Summarizing all the above, the normal derivative of the function f can be finally written as

$$\frac{\partial f}{\partial n} = \left(\frac{\partial f}{\partial R}\cos\Theta - \frac{\partial f}{\partial \Theta}\frac{\sin\Theta}{R}\right)n_\xi + \left(\frac{\partial f}{\partial R}\sin\Theta + \frac{\partial f}{\partial \Theta}\frac{\cos\Theta}{R}\right)n_\eta + \frac{\partial f}{\partial \zeta}n_\zeta. \tag{C.4}$$

References

Abramowitz, M., Stegun, I.A., 1964. Handbook of mathematical functions: With formulas, graphs, and mathematical tables. National Bureau of Standards.

Babarit, A., Delhommeau, G., 2015. Theoretical and numerical aspects of the open source BEM solver NEMOH. Proceeding of the 11th European Wave and Tidal Energy Conference, Nantes, France.

Bennetts, L.G., Squire, V.A., 2009. Wave scattering by multiple rows of circular ice floes. J Fluid Mech 639, 213–238.

Black, J.L., 1975. Wave forces on vertical axisymmetric bodies. J Fluid Mech 67 (2), 369–376.

Chakrabarti, S.K., 2001. Response due to moored multiple structure interaction. Mar. struct. 14 (1–2), 231–258.

Chau, F.P., 1989. The second order velocity potential for diffraction of waves by fixed offshore structures.. University College London.

Child, B.F.M., Venugopal, V., 2010. Optimal configurations of wave energy device arrays. Ocean Eng. 37 (16), 1402–1417.

Cong, P.-W., Gou, Y., Teng, B., 2012. A new approach to low-frequency QTF and its application in predicting slow drift force. Ocean Eng. 53, 25–37.

Dai, Y.S., Duan, W.Y., 2008. Potential flow theory of ship motions in waves. National Defense Industry Publication.

Eatock Taylor, R., Chau, F.P., 1992. Wave diffraction theory-some developments in linear and nonlinear theory. J. Offshore Mech. Arct. Eng. 114, 185–194.

Fenton, J.D., 1978. Wave forces on vertical bodies of revolution. J Fluid Mech 85 (2), 241–255.

Flavià, F.F., Babarit, A., Clément, A.H., 2017. On the numerical modelling and optimization of a bottom-referenced heave-buoy array of wave energy converters. Int. J. Mar. Energy 19, 1–15.

Flavià, F.F., McNatt, C., Rongère, F., Babarit, A., Clément, A.H., 2016. Computation of the Diffraction Transfer Matrix and the Radiation Characteristics in the open-source BEM code NEMOH. Proceeding of the 35th International Conference on Offshore Mechanics and Arctic Engineering, Busan, Korea, Vol. 49972. American Society of Mechanical Engineers.V006T09A014

Flavià, F.F., McNatt, C., Rongère, F., Babarit, A., Clément, A.H., 2018. A numerical tool for the frequency domain simulation of large arrays of identical floating bodies in waves. Ocean Eng. 148, 299–311.

Flavià, F.F., Meylan, M.H., 2019. An extension of general identities for 3d water-wave diffraction with application to the diffraction transfer matrix. Appl. Ocean Res. 84, 279–290.

Goo, J.-S., Yoshida, K., 1990. A numerical method for huge semisubmersible responses in waves. Transactions-Society of Naval Architects and Marine Engineers 98, 365–387.

Göteman, M., 2017. Wave energy parks with point-absorbers of different dimensions. J Fluids Struct 74, 142–157.
Göteman, M., Engström, J., Eriksson, M., Isberg, J., 2015. Fast modeling of large wave energy farms using interaction distance cut-off. Energies 8 (12), 13741–13757.
Hulme, A., 1983. A ring-source/integral-equation method for the calculation of hydrodynamic forces exerted on floating bodies of revolution. J Fluid Mech 128, 387–412.
John, F., 1950. On the motion of floating bodies II. simple harmonic motions. Commun Pure Appl Math 3 (1), 45–101.
Kagemoto, H., Yue, D.K.P., 1986. Interactions among multiple three-dimensional bodies in water waves: an exact algebraic method. J Fluid Mech 166, 189–209.
Kashiwagi, M., 2000. Hydrodynamic interactions among a great number of columns supporting a very large flexible structure. J Fluids Struct 14 (7), 1013–1034.
Kashiwagi, M., 2001. Wave-induced local steady forces on a column-supported very large floating structure. Proceeding of the 11th International Offshore and Polar Engineering Conference, Stavanger, Norway. International Society of Offshore and Polar Engineers.
Kashiwagi, M., 2003. Practical hydrodynamics of floating bodies, volume 1: numerical computation methods for body-oscillation problems. Japan Society of Naval Architects.
Kashiwagi, M., 2017. Hydrodynamic interactions of multiple bodies with water waves. Int. J. Offshore Polar Eng. 27 (02), 113–122.
Kashiwagi, M., Kohjo, T., 1995. A calculation method for hydrodynamic interactions of multiple bodies supporting a huge floating body (in japanese), 247–254.
Kim, M.H., Yue, D.K.P., 1989. The complete second-order diffraction solution for an axisymmetric body. part 1. monochromatic incident waves. J Fluid Mech 200, 235–264.
Lau, S.M., Hearn, G.E., 1989. Suppression of irregular frequency effects in fluid–structure interaction problems using a combined boundary integral equation method. Int J Numer Methods Fluids 9 (7), 763–782.
Lee, C.H., 1995. WAMIT theory manual. Technical Report. Department of Ocean Engineering, Massachusetts Institute of Technology.
Lee, C.H., Newman, J.N., 2005. Computation of wave effects using the panel method. Numerical Models in Fluid Structure Interaction 42, 211–251.
Liang, H., Ouled Housseine, C., Chen, X.B., Shao, Y., 2020. Efficient methods free of irregular frequencies in wave and solid/porous structure interactions. J Fluids Struct 98, 103130.
Liu, Y., 2019. HAMS: A frequency-domain preprocessor for wave-structure interactions – theory, development, and application. J Mar Sci Eng 7 (3), 81.
Liu, Y., Yoshida, S., Hu, C., Sueyoshi, M., Sun, L., Gao, L., Cong, P., He, G., 2018. A reliable open-source package for performance evaluation of floating renewable energy systems in coastal and offshore regions. Energy Convers. Manage. 174, 516–536.
McIver, P., 1984. Wave forces on arrays of floating bodies. J Eng Math 18 (4), 273–285.
McIver, P., Evans, D.V., 1984. The occurrence of negative added mass in free-surface problems involving submerged oscillating bodies. J Eng Math 18 (1), 7–22.
McNatt, J.C., Venugopal, V., Forehand, D., 2013. The cylindrical wave field of wave energy converters. Int. J. Mar. Energy 3, e26–e39.
McNatt, J.C., Venugopal, V., Forehand, D., 2015. A novel method for deriving the diffraction transfer matrix and its application to multi-body interactions in water waves. Ocean Eng. 94, 173–185.
Meylan, M., 2007 (accessed on Oct. 12, 2020). Wikiwaves. https://wikiwaves.org/Graf%27s_Addition_Theorem.
Ohkusu, M., 1974. Hydrodynamic forces on multiple cylinders in waves. Proceedings of International Symposium on the Dynamics of Marine Vehicles and Structures in Waves, London, England. Institute of Mechanical Engineers.
Ohmatsu, S., 1983. A new simple method to eliminate the irregular frequencies in the theory water wave radiation problems. Technical Report. Papers of Ship Research Institute.
Penalba, M., Kelly, T., Ringwood, J., 2017. Using NEMOH for modelling wave energy converters: A comparative study with WAMIT. Proceeding of the 12th European Wave and Tidal Energy Conference (EWTEC2017), Cork, Ireland.
Peter, M.A., Meylan, M.H., 2004. The eigenfunction expansion of the infinite depth free surface green function in three dimensions. Wave Motion 40 (1), 1–11.
Peter, M.A., Meylan, M.H., 2004. Infinite-depth interaction theory for arbitrary floating bodies applied to wave forcing of ice floes. J Fluid Mech 500, 145–167.
Siddorn, P., Taylor, R.E., 2008. Diffraction and independent radiation by an array of floating cylinders. Ocean Eng. 35 (13), 1289–1303.
Simon, M.J., 1982. Multiple scattering in arrays of axisymmetric wave-energy devices. part 1. a matrix method using a plane-wave approximation. J Fluid Mech 120, 1–25.
Spring, B.H., Monkmeyer, P.L., 1974. Interaction of Plane Waves with Vertical Cylinders. Proceeding of the 14th International Conference on Coastal Engineering, Copenhagen, Denmark, pp. 1828–1847.
Sun, L., Stansby, P., Zang, J., Moreno, E.C., Taylor, P.H., 2016. Linear diffraction analysis for optimisation of the three-float multi-mode wave energy converter M4 in regular waves including small arrays. Journal of Ocean Engineering and Marine Energy 2 (4), 429–438.
Teng, B., 2016. A Higher-order Boundary Element Method for Wave-structure Interactions. In: Teng, B. (Ed.), Analysis theories and applications of wave-structure interactions (a special proceeding dedicated to Prof. Li, Y. C. on his eighty birthday). Ocean Press, Beijing, China.
Teng, B., Cong, P.W., 2017. A novel decomposition of the quadratic transfer function (QTF) for the time-domain simulation of non-linear wave forces on floating bodies. Appl. Ocean Res. 65, 112–128.
Teng, B., Eatock Taylor, R., 1995. New higher-order boundary element methods for wave diffraction/radiation. Appl. Ocean Res. 17 (2), 71–77.
Twersky, V., 1952. Multiple scattering of radiation by an arbitrary configuration of parallel cylinders. J. Acoust. Soc. Am. 24 (1), 42–46.
Watson, G.N., 1995. A treatise on the theory of bessel functions. Cambridge University Press.
Zheng, S., Zhang, Y., Iglesias, G., 2018. Wave–structure interaction in hybrid wave farms. J Fluids Struct 83, 386–412.
Zheng, S., Zhang, Y., Iglesias, G., 2020. Power capture performance of hybrid wave farms combining different wave energy conversion technologies: the H-factor. Energy 117920.
Zhong, Q., Yeung, R.W., 2019. Wave-body interactions among energy absorbers in a wave farm. Appl Energy 233, 1051–1064.